to be of the same order of magnitude makes one suspect that they may be proved to be exactly equal, at least in a certain limit. Indeed, in a self-consistent model, such as that discussed by Cutkosky,[3] the ratio between the mixing angles is in principle fixed by the self-consistency requirement.

In conclusion, the arguments presented above seem to prove that the predictions of SU_3 symmetry are not even qualitatively consistent with the experimental observations if no vector mesons other than the members of the octet are assumed to exist. The inconsistencies can be removed by the introduction of a unitary singlet vector meson for which some empirical support is available. However, it might well be that other more complicated interactions, such as the exchange of members of other multiplets, could play an important role.

ACKNOWLEDGMENTS

It is a pleasure to thank Dr. R. E. Cutkosky who not only suggested the general trend of the present investigation, but also has guided me through the many details of calculation. I should also like to express my gratitude to Dr. P. Tarjanne for what I have learned from him about the group-theoretical aspects of SU_3 symmetry, and to the Carnegie Institute of Technology, Pittsburgh, for granting me the opportunity of joining the Physics department there for a year. Finally, I thank my wife for drawing the curves and for pointing out to me several errors in the numerical calculations.

PHYSICAL REVIEW VOLUME 131, NUMBER 5 1 SEPTEMBER 1963

Analysis of Y_0^* (1520) and Determination of the Σ Parity*

MASON B. WATSON,† MASSIMILIANO FERRO-LUZZI,‡ AND ROBERT D. TRIPP
Lawrence Radiation Laboratory, University of California, Berkeley, California
(Received 15 March 1963)

The interaction of K^- mesons on protons resulting in elastic and charge-exchange scattering and hyperon production are reported for a range of momenta from 250 to 513 MeV/c. About 10 000 events obtained in the Lawrence Radiation Laboratory's 15-in. bubble chamber were analyzed. Differential and total cross sections for all channels are examined. For $\Sigma^+\pi^-$, $\Sigma^0\pi^0$, and $\Lambda\pi^0$ production, polarization measurements are also available. A resonant state is identified with a mass 1519 MeV and a full width $\Gamma=16$ MeV, decaying into $\bar{K}N$, $\Sigma\pi$, and $\Lambda\pi\pi$ in the branching ratio 30:55:15, respectively. The resonance is found to have isotopic spin 0 and spin $\frac{3}{2}$, and its parity is that of the $\bar{K}N$ $D_{3/2}$ state. By use of the polarization arising from the $D_{3/2}-S$-wave interference, a strong argument for negative $KN\Sigma$ parity is obtained. All the data are fitted to a model based on a Breit-Wigner resonant amplitude and nonresonant S, P, and D amplitudes, parametrized by constant scattering lengths. An extensive search for χ^2 minima was done on an IBM-7090 computer under various assumptions for the spin and parity of the resonance. Only the $D_{3/2}$ possibility in both K^-p and $\Sigma\pi$ states yields a satisfactory (43% probability) fit. A $D_{5/2}$ K^-p resonance (with $\Sigma\pi$ in $F_{5/2}$) is the nearest alternative possibility, with a likelihood of less than 1% of fitting the data.

I. INTRODUCTION

BELOW 300 MeV/c the K^-p interaction is strongly dominated by S waves. All channels have been found to be satisfactorily described by the S-wave zero-effective-range approximation.[1] Above 300 MeV/c, higher partial waves begin to exhibit themselves in a spectacular fashion. Previous to this experiment, an analysis of 140 interactions at 400 MeV/c in the 15-in. liquid-hydrogen bubble chamber indicated a large $\cos^2\theta$ term in the elastic angular distribution.[2] With this guidance, a much more detailed study of this region was begun in 1960. Over 10 000 events have been analyzed at K^- laboratory momenta of about 300, 350, 400, 440, and 510 MeV/c and form the source of the data presented here. Apart from the addition of 1000 more K^-p elastic scatters and the inclusion of a "beam averaging" procedure, the data are essentially the same as reported in preliminary form earlier.[3] Computer fits to the final data presented here yield resonance parameters very similar to those found in the precomputer analysis.

In Sec. II we discuss the K^- beam, and in Sec. III, the scanning and measuring procedure. The results of the measurements and remarks on experimental biases appear in Sec. IV. A simplified discussion of the resonance is found in Secs. V and VI, where we establish the properties of the resonance and develop the argument

* This work was done under the auspices of the U. S. Atomic Energy Commission.
† Present address: Aerospace Corporation, El Segundo, California.
‡ Present address: CERN, Geneva 23, Switzerland.
[1] W. E. Humphrey and R. R. Ross, Phys. Rev. **127**, 1305 (1962).
[2] L. W. Alvarez, in *Proceedings of Ninth International Annual Conference on High-Energy Physics, Kiev, 1959* (Academy of Sciences, Moscow, 1960), and Lawrence Radiation Laboratory Report UCRL-9354, 1960 (unpublished); also P. Nordin, Phys. Rev. **123**, 2168 (1961).
[3] M. Ferro-Luzzi, R. D. Tripp, and M. B. Watson, Phys. Rev. Letters **8**, 28 (1962); R. D. Tripp, M. B. Watson, and M. Ferro-Luzzi, *ibid.* **8**, 175 (1962).

concerning the $KN\Sigma$ parity. The least-squares computer analysis is formulated in Sec. VII, and the results of the computer analysis under various assumptions for the quantum numbers of the resonance appear in Sec. VIII. In Sec. IX we discuss the approximations made in the computer analysis and the extent to which the Σ-parity determination depends on these assumptions.

II. BEAM

The beam setup was designed and built by Murray and has been reported elsewhere.[4] Here we shall recall only its main features.

The beam was designed to provide K^- mesons with momenta up to 800 MeV/c. The momenta considered in this experiment were obtained by degrading the original beam. The K^- mesons were produced by the maximum-energy proton beam of the Bevatron striking a copper target. The beam was extracted from the target at 0 deg, where the π^-/K^- ratio was approximately 500 to 1. Once the beam was outside the Bevatron magnet structure, two stages of electrostatic separation were employed to select a narrow momentum interval while separating K^- from π^-. Crossed electric and magnetic fields were adjusted so that the K^- mesons were undeflected, while the π^- were deflected vertically. The deflection of the π^- image at the first mass-resolving slit was about $\frac{1}{2}$ in. from the K^- image. At that point, the K^- were directed through a $\frac{1}{8}$-in.$\times 2\frac{1}{4}$-in. opening into the second stage, while the π^- were arrested in the lead walls of the slit. The success of this method depends critically on the separation of the π^- and K^- images, which is limited by the electric and magnetic fields obtainable in the separators.

This experiment was the first to utilize the heated-glass-cathode technique due to Murray.[5] This enabled us to reach a 50% higher electric-field gradient than was possible with previous separators. During normal operation 450 kV applied across a 2-in. gap between parallel plates in both of the identical 10-ft separators yielded a gradient of approximately 90 kV/cm.

At the first slit the beam momentum was 800 MeV/c, with a spread of 1%, coherently focused across the slit in the horizontal plane. A beryllium wedge was placed in the beam so that the high-momentum side traversed the thick end, while the low-momentum side was only slightly slowed by the pointed end. After wedging, the momentum spread was reduced to $\pm\frac{1}{2}\%$. The second stage was then essentially free of chromatic aberrations.

There were two main causes of K^- loss. The length of the beam was $\sim$75 ft, so that only $\approx$2.1% of the 800-MeV/c K mesons produced at the target lived long enough to reach the absorber in front of the bubble chamber. The second cause of K^- loss was through absorption in the copper absorber, which served to degrade the incident momentum. This loss depended on the amount of absorber, varying in our case between a factor of 4 and 5. This degrading also increased the relative momentum spread as the central momentum decreased.

At 800 MeV/c, the K flux in the bubble chamber was $15K^-$ per 10^{11} protons striking the target. At 400 MeV/c, there were about three K^- entering the chamber on each picture. There were approximately 30% background tracks, half of which were π^-. The π^- contamination was determined from π^--p scatterings observed in the chamber. Since π^- are not slowed down at the same rate as K^-, the π^- had a systematically higher momentum. The difference between the mean momenta of the K^- and π^- ranged from 100 MeV/c at a K^- momentum of 510 MeV/c to 200 MeV/c at 300 MeV/c.

The median K^- momenta for the various exposures were 292, 350, 387, 392, 434, and 513 MeV/c. The two exposures at 387 and 392 MeV/c are combined on occasion, as they differed by a small amount, and referred to as the 390 MeV/c run.

III. SCANNING AND MEASURING

The film was scanned for interactions and decays by a team of five technicians. When an event was found, it was classified according to the number of prongs leaving the production vertex. All V's that could have been associated and all subsequent decays were recorded. There were eight possible topologies:

1. zero prongs	0
2. zero prongs plus a V	0V
3. one prong	1
4. two prongs	2
5. two prongs with a positive decay	2+
6. two prongs with a negative decay	2−
7. two prongs plus a V	2V
8. three prongs	3

The efficiency for detection of an event varies, of course, with the type of event and its position in the chamber. To eliminate poorly illuminated areas in the chamber, a "fiducial volume" was chosen which provided a margin on all sides.

The 0- and 1-prong events were not used in the analysis and will be neglected.

In order to evaluate the scanning efficiency, about 25% of the film was scanned twice. Table I shows the results of the comparison. The efficiency for detecting the events studied appears to be very high, obviating

TABLE I. Scanning efficiencies for the different topologies, obtained from a double scan of $\approx$25% of the film.

Topology	0V	2	2±	2V	3
Efficiency (%)	98.3	97.1	99.2	100	97.0

[4] P. Bastien, O. I. Dahl, J. J. Murray, M. B. Watson, R. G. Ammar, and P. Schlein, in *Proceedings of the International Conference on Instrumentation for High-Energy Physics at Berkeley, 1960* (Interscience Publishers, Inc., New York, 1961), p. 299–301.

[5] Joseph J. Murray, in *Proceedings of the International Conference on Instrumentation for High-Energy Physics at Berkeley, 1960* (Interscience Publishers, Inc., New York, 1961), pp. 25–33.

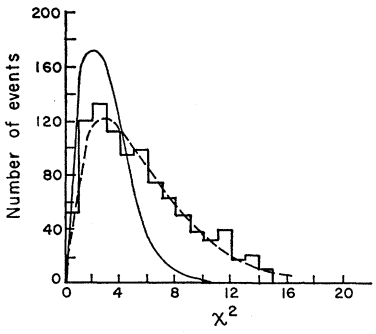

FIG. 1. Distribution of the χ^2 in the fit of 948 elastic scatterings.

corrections for scanning losses in computing cross sections.

A sketch was made for each event selected to be measured. This sketch served to specify to the measurer which two of the four pictures of each frame presented the best stereo pair. Once sketched, the event was measured by using a "Franckenstein." This machine is essentially a projection microscope which digitizes in Cartesian coordinates several points along each track of the event in the photograph. The coordinates are punched on IBM cards along with appropriate reference points and event-identifying information. The cards served as input to the event-reconstruction computer programs.

Each event was reconstructed, track by track in space, from the digitized input cards by the IBM-7090 program PACKAGE.[6] This is the standard program in use by the Alvarez Group for event reconstruction and kinematical analysis. The same program subjects the measured variables on each track to the constraints of momentum and energy conservation for the entire event. The measured quantities were adjusted to give the best fit satisfying the constraints, as measured by a χ^2 calculated by the program. In most cases each event was subjected to several different interpretations. Usually, the χ^2 value unambiguously selected one interpretation.

In order to study the χ^2 distribution, a large group of elastic scatterings was chosen randomly. Since usually all tracks are measurable in such events, the constraints of momentum and energy conservation left the "fit" four times overdetermined. The χ^2 for such a case should have a mean of 4. Figure 1 shows the observed χ^2 distribution and a theoretical curve normalized to the correct number of events for four degrees of freedom (solid curve). The observed distribution appears to be more spread out than expected. The dashed curve corresponds to the case in which the error assignments are about 20% underestimated; this last fit is quite good, indicating that no serious distortions exist but only a misassignment of error magnitudes.

As a measure of the contribution to the χ^2 discrepancy by each measured variable, the "pull" quantities $P_i(x)$ were examined. The $P_i(x)$ are defined by

$$P_i(x^*)=(x_i^*-x_i^{\text{meas}})/\langle(x_i^*-x_i^{\text{meas}})^2\rangle^{1/2},$$

where x_i^* is the adjusted value of a variable corresponding to the measured value x_i^{meas}. The pull quantities should have a mean value of zero and a standard deviation of one if no systematic errors are made and if the measurement errors are correctly assigned. These quantities are discussed in detail in connection with the

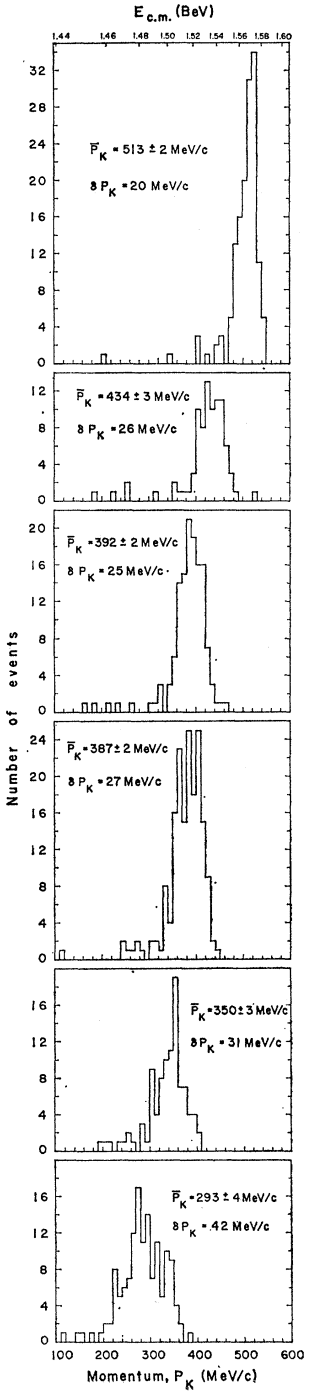

FIG. 2. K^- momentum spectra from fitted τ decays at the six exposure settings. Here $\bar{P}_k$ is the median momentum, and δP_k the standard deviation. There were 134 events at 293 MeV/c, 97 at 350, 166 at 387, 128 at 392, 81 at 434, and 59 at 513.

TABLE II. Cross sections for the different K^- momenta settings (in MeV/c) for K^-+p reactions.

Reaction products	Cross sections (mb) $P_K=293\pm42$	350 ± 31	387 ± 30	392 ± 30	$390^a\pm30$	434 ± 26	513 ± 20
K^-+p	48.2 ±4.2	34.0 ±3.2	31.9 ±2.5	34.0 ±3.0	32.7 ±1.8	30.6 ±3.4	26.5 ±3.3
$\bar{K}^0+n$	8.0 ±1.2	5.1 ±1.1	8.1 ±1.0	10.0 ±1.0	8.8 ±0.7	6.0 ±1.2	3.6 ±0.6
$\Sigma^++\pi^-$	13.6 ±1.4	10.6 ±1.4	11.4 ±1.0	14.0 ±1.4	12.5 ±0.8	8.2 ±0.9	7.5 ±1.1
$\Sigma^-+\pi^+$	10.0 ±1.1	6.9 ±1.0	6.0 ±0.6	8.3± 0.9	6.9 ±0.5	6.1 ±0.7	4.9 ±0.8
$\Sigma^0+\pi^0$ [b]	5.2 ±0.9	6.3 ±1.4	6.9 ±0.9	6.4 ±1.0	6.7 ±0.6	4.9 ±1.3	1.7 ±0.3
$\Lambda+\pi^0$	5.2 ±0.9	4.5 ±1.0	2.9 ±0.5	3.3 ±0.6	3.1 ±0.3	3.2 ±0.7	1.6 ±0.4
$\Lambda+\pi^0+\pi^0$ [c]	0.3 ±0.2	1.9 ±0.6	1.2 ±0.4	1.8 ±0.3	1.5 ±0.2	0.8 ±0.4	1.1 ±0.3
$\Lambda+\pi^++\pi^-$	0.15±0.10	0.9 ±0.3	1.2 ±0.3	2.4 ±0.4	1.6 ±0.2	1.5 ±0.4	2.0 ±0.4
$\Sigma^0+\pi^++\pi^-$	0 ±0.08	0 ±0.09	0.08±0.05	0.06±0.06	0.07±0.06	0 ±0.08	0.3 ±0.15
$\Sigma^++\pi^-+\pi^0$	0 ±0.05	0.06±0.06	0.09±0.05	0.21±0.10	0.11±0.04	0.18±0.11	0.20±0.12
$\Sigma^-+\pi^++\pi^0$	0.05±0.05	0 ±0.06	0.03±0.03	0.17±0.09	0.12±0.05	0 ±0.06	0.14±0.10
Total	90.7 ±4.9	70.2 ±4.2	69.6 ±3.2	80.6 ±4.0	73.8 ±2.3	61.5 ±4.1	49.5 ±3.7
$(\Sigma\pi)_{I=0}$	15.6 ±2.7	18.9 ±4.2	20.7 ±2.7	19.2 ±3.0	20.1 ±1.8	14.7 ±3.9	5.1 ±0.9
$(\Sigma\pi)_{I=1}$	13.2 ±2.5	4.9 ±3.3	3.6 ±2.2	9.5 ±2.6	6.0 ±1.4	4.5 ±2.8	9.0 ±1.5
$\pi\chi^2$	35.7	25.6	21.4	20.8	20.9	17.3	13.0

[a] Combined runs 387 and 392 MeV/c.
[b] Derived from $\sigma(\Sigma^0\pi^0)=\sigma(\Sigma^0\pi^0+\Lambda\pi^0\pi^0)-\frac{1}{2}\sigma(\Lambda\pi^+\pi^-)$.
[c] Derived from phase-space considerations; as they stand they violate charge independence when compared with $\Lambda\pi^+\pi^-$.

predecessor program to PACKAGE called KICK.[6] When these quantities are plotted for all the measured variables, the curves show normal distributions having in each case a mean value nonsignificantly shifted from zero and widths indicating an underestimate of the measurement errors by about 20%. At no point in the experiment was a major dependence placed on the proper distribution of χ^2, only on relative values. The errors introduced by deviations in the distribution of χ^2 function and the pull quantities were believed to be negligible compared with the statistical uncertainties inherent in the data. The output of PACKAGE was in the form of a binary magnetic tape which served as input to a series of short Fortran EXAMIN routines. These calculated and organized the pertinent physical quantities not directly measured.

Finally, but not less important, there was the examination on the scanning table of all events that gave "bad fits." These were events where unexpected strong distortions in the chamber or bad illumination were responsible for completely false measurements. Furthermore, unnoticed small scatterings or just wrong measurements also went into this category. Through repeated measurements with special precautions (not excluding hand analysis of the events), we were eventually successful in assigning an interpretation to all events.

IV. RESULTS OF THE MEASUREMENTS

A. τ Decays and Path Length

Events of the type $K^-\rightarrow\pi^++\pi^-+\pi^-$ (τ decay) have the advantage over the one-prong decays of being very easily identifiable in the chamber and of allowing an accurate measure of the incident K momentum. Therefore, they provide a far better measurement of the incoming K flux than would the much more numerous one-prong decays.

The incident K^- momentum determined from these events had a typical uncertainty of ±5 MeV/c. Figure 2 shows the K^- momentum spectra obtained from the τ decay at each momentum setting. By use of a K^- lifetime of 1.224×10^{-8} sec and a τ-decay branching ratio of 5.77%,[7] the flux of K^- at each interval was determined by the number of τ decays observed. The momentum spread of all incoming K's is identical to the decay spectrum after correction for time dilation. This correction consists of weighing the number of τ's in each interval around P_k by a factor equal to $P_k/\bar{P}_k$, where $\bar{P}_k$ denotes the median momentum for the whole run.

As expected, the shape of the spectrum at each momentum interval is approximately Gaussian, with a low-momentum tail. All interactions and τ decays whose fitted incident momentum was 100 MeV/c or more below the median $\bar{P}_k$ were discarded. Such events were usually not part of the low-momentum tail, but resulted from "off-beam" particles mainly produced in large-angle scatterings in the absorber or final mass-resolving slit.

The value of the median momentum $\bar{P}_k$ obtained from the τ decays was then used in fitting all other types of events. This was done by averaging the measured incident momentum of each event with $\bar{P}_k$, the two momenta being weighted by the measurement error and by the variance δP_k of the τ-decay momentum spectrum, respectively. Each event was fitted both with and without this "beam-averaging" procedure, in order to recognize and eliminate off-beam events. The beam-averaging procedure allowed a more precise determina-

[6] See, for example, A. H. Rosenfeld, in *Proceedings of the International Conference on High-Energy Accelerators and Instruments* (CERN, Geneva, 1959), pp. 533–541. This describes the separate PANG-KICK system. For more details see Reference Manual for KICK IBM Program, Lawrence Radiation Laboratory Report UCRL-9099, 1961 (unpublished).

[7] The lastest summary of $K^\pm$ branching ratios yields 5.7±0.2%. See F. S. Crawford in *Proceedings of the 1962 International Conference on High Energy Physics at CERN* (CERN, Geneva, 1962).

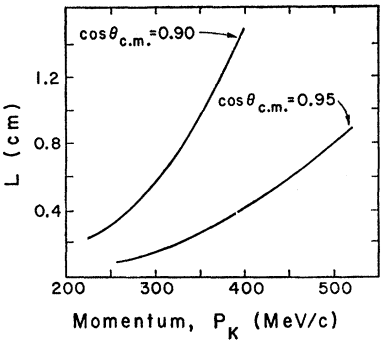

FIG. 3. Length of the recoil proton in elastic scatters for fixed c.m. scattering angles ($\theta_{c.m.}$) as a function of the incident K^- laboratory momentum. The $\cos\theta_{c.m.}=0.90$ cutoff was adopted.

tion of the incident momentum than possible by direct measurement only. For example, when the incident track was very short or hidden by other tracks, direct measurement often gave unlikely values.

Finally, all the τ decays have also been merged to give a single momentum distribution over the whole explored region. This over-all path length was then used to calculate values of the cross sections for momentum intervals smaller than those covered by the individual runs.

Table II gives values of the total and partial cross sections for each run; the values for smaller momentum intervals are displayed in Figs. 26 through 29.

B. Elastic Scattering

Elastic scatterings represent roughly one-half of all interactions. Those chosen for analysis were found entirely in the "two-prong" events. Obviously, for small-angle scatterings in which the recoil protons carry off little momentum, there is some minimum angle beyond which the protons are no longer visible. Such an event would be classified as a "one-prong" and lost among the thousands of K^- decays. Long before the recoil becomes completely invisible, the efficiency for observing the proton stub drops considerably. Rather than attempt to evaluate the detection efficiency, which varies rapidly with scattering angle, we eliminated all events with cosines of the scattering angle greater than 0.9 in the center of mass. Figure 3 shows the length of the recoil proton versus K^- momentum for center-of-mass scattering cosines of 0.9 and 0.95. The 0.9 cutoff should guarantee a high scanning efficiency. A uniform cutoff for all momentum intervals was desirable to simplify merging the different runs. For the higher momentum intervals, the 0.9 cutoff may seem too stringent. However, the pion contamination in the beam leads to π^--proton scatterings which at forward angles cannot be separated from K^--proton scatterings. For cosines less than 0.9 this ambiguity essentially disappears. Thus, 0.9 was chosen both to eliminate short-recoil scanning losses and the π^--p scattering contamination.

If the plane of an elastic scattering were vertical, the camera might see only the edge of the plane. Thus, we might expect a scanning bias against detecting events in which the plane of scattering is nearly vertical. There are two factors tending to reduce the effect of this bias. The bubble chamber has four cameras. Whereas one camera might view only the edge of the plane, the event should be clearly seen in one of the other three views. Also, the magnetic field in the chamber deflects the scattered K^- mesons and protons in opposite directions. Therefore, even an edge-on view usually appears V shaped. Small-angle scatterings with short recoils and little momentum loss by the K^- meson would most likely be missed. Figure 4 shows the distribution of events for various orientations of the plane of scattering. This distribution should be and is isotropic. The $\cos\theta=0.9$ cutoff is stringent enough to eliminate this source of trouble.

Figure 5 shows the distribution of errors for the incident K^--meson momentum resulting from the fit.

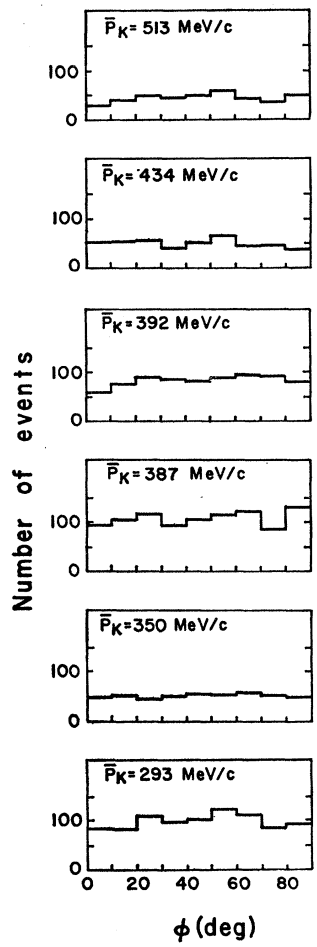

FIG. 4. Distribution of elastic scatterings versus the angle ϕ, where

$$\cos\phi=\frac{(\mathbf{K}_{in}\times\mathbf{K}_{out})\cdot(\mathbf{K}_{in}\times\hat{z}_{axis})}{|\mathbf{K}_{in}\times\mathbf{K}_{out}||\mathbf{K}_{in}\times\hat{z}_{axis}|}.$$

Here $\mathbf{K}_{in}$ and $\mathbf{K}_{out}$ are vectors in the incident and outgoing K directions, and the z axis is vertical; ϕ is 0 deg for a vertical scattering plane. The distributions are folded about 90, 180, and 270 deg.

TABLE III. Least-squares fits to the angular distributions for K^-p.

$\bar{P}_K$ (MeV/c)	σ (mb)	Order of fit	Expansion coefficients (mb/sr) C_0	C_1	C_2	C_3	C_4	χ^2	Expected χ^2	Confidence level (%)
293	48.2±4.2	0	3.78±0.13					11.8	18	84.7
		1	3.79±0.13	0.08±0.23				11.7	17	80.0
		2	3.81±0.19	0.07±0.24	−0.10±0.46			11.6	16	74.4
		3	3.78±0.19	−0.50±0.57	0.09±0.49	1.06±0.98		10.5	15	75.3
		4	3.62±0.24	−0.32±0.59	1.93±1.67	0.56±1.07	−2.43±2.10	9.1	14	83.1
350	34.0±3.2	0	2.36±0.11					18.8	9	2.5
		1	2.40±0.11	0.41±0.22				15.3	8	5.9
		2	2.10±0.16	0.60±0.23	1.15±0.45			8.7	7	27.5
		3	2.05±0.17	0.02±0.52	1.43±0.50	1.20±0.95		7.1	6	31.2
		4	2.12±0.20	−0.12±0.56	0.50±1.53	1.58±1.12	1.35±2.09	6.7	5	24.4
390	32.7±1.8	0	2.16±0.06					214.4	18	$<10^{-5}$
		1	2.19±0.06	0.36±0.12				205.4	17	$<10^{-5}$
		2	1.53±0.07	0.87±0.13	3.12±0.23			25.2	16	7.0
		3	1.50±0.08	0.31±0.26	3.35±0.25	1.19±0.49		19.2	15	21.4
		4	1.41±0.09	0.48±0.28	4.61±0.76	0.75±0.55	−1.83±1.04	16.1	14	31.3
434	30.6±3.4	0	2.12±0.10					21.7	9	0.9
		1	2.14±0.10	0.23±0.19				20.4	8	1.0
		2	1.82±0.14	0.37±0.20	1.23±0.41			11.3	7	13.9
		3	1.84±0.15	0.63±0.46	1.14±0.43	−0.55±0.85		10.8	6	8.8
		4	1.95±0.19	0.46±0.48	−0.31±1.38	−0.09±0.95	2.06±1.87	9.6	5	8.7
513	26.5±3.3	0	1.75±0.10					49.8	18	0.008
		1	2.01±0.11	1.17±0.19				12.7	17	73.6
		2	1.82±0.15	1.33±0.21	0.72±0.40			9.5	16	86.7
		3	1.84±0.16	1.52±0.45	0.63±0.46	−0.40±0.81		9.2	15	87.8
		4	2.00±0.19	1.14±0.51	−1.20±1.33	0.42±0.98	2.54±1.73	7.1	14	93.5

The double peaks can be explained as follows: For small angles the recoil-proton momenta are well defined, since the protons stop in the chamber. For very large angles the scattered K^- mesons stop. Since a momentum derived from range measurement is much more accurate than momentum obtained via curvature, both very forward and very backward scatterings yield better fits. In fact, an exact correspondence between stopping tracks and the first peak was found.

In order to calculate cross sections for elastic scattering, the number of events with $\cos\theta \leqslant 0.9$ must be corrected to include all angles. This was done by fitting a power series in $\cos\theta$ to each angular distribution; the total number of events was then obtained by integrating the best-fit curve.

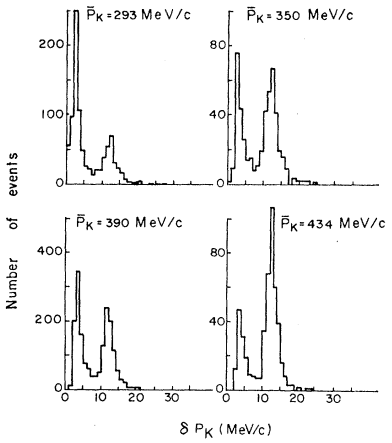

FIG. 5. Incident-K^- fitted momentum error for elastic scatterings. The double peaks are due to the different accuracies attainable in the momentum determinations of the scattered particles for stopping and leaving tracks.

Figure 6 shows the differential cross sections for each of the momentum settings individually. These distributions were fitted by a least-squares procedure to a polynomial of the form

$$d\sigma/d\Omega = C_0 + C_1\cos\theta + C_2\cos^2\theta + \cdots + C_n\cos^n\theta,$$

where θ is the c.m. angle between the incident and scattered K^- mesons.

The results of these fits for orders $n=0$ through 4 are displayed in Table III, together with the values obtained for the elastic-scattering cross sections.

The optical theorem relates the imaginary part of the forward-scattering amplitude to the total cross section. The square of the imaginary part gives a lower limit to the differential cross section in the forward direction. The square of this imaginary part is shown for each distribution in Fig. 6. Notice that in all cases the real part is consistent with zero.

C. Sigma Production

Most of these events were found among the "two prongs with a decay" topology, but severe biases would have occurred if the analysis had been restricted to only this topology.

Examination of the kinematics of sigma production for this range of K^- momenta reveals a disturbing fact. Sigmas of both signs produced backwards in the center

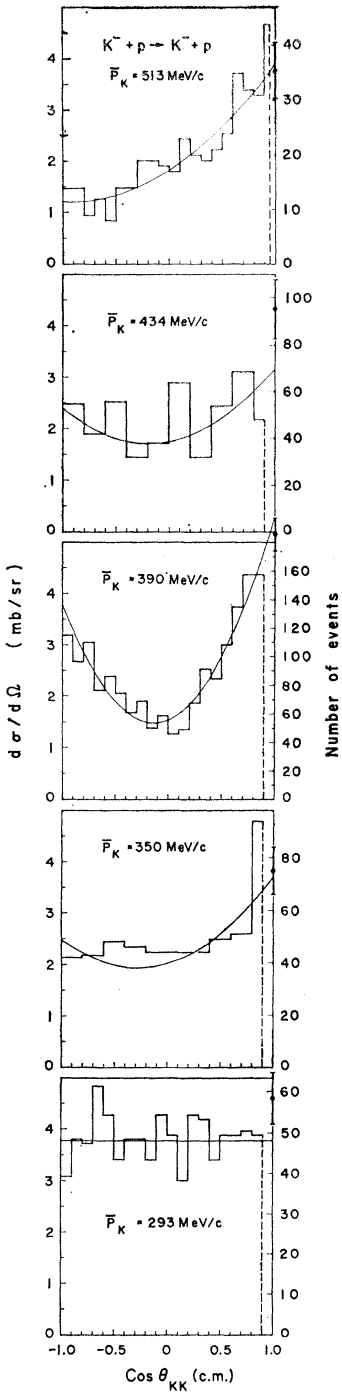

FIG. 6. Differential cross sections for elastic scatterings; θ_{KK} is the angle between the incident and scattered K^-. The curves are best fits to the data. The points on the right-hand ordinate represent the square of the imaginary part of the forward-scattering amplitude, as obtained from the optical theorem.

of mass have such low laboratory momenta that they stop, and, hence, decay or interact, *before* making a visible track. Such an event would be recorded as a two-prong event or possibly even as one prong plus V i.e.,

$$K^-+p\rightarrow\Sigma^-+\pi^+,\ \Sigma^-+p\rightarrow\Lambda+n,\ \Lambda\rightarrow p+\pi^-.$$

The protonic decay mode of the Σ^+ hyperon may appear to be an elastic scattering if the production-pion ionization is not examined carefully or if the track is dipping steeply. In the examination of two-prong events during the analysis of the elastic scatterings, a group of events was found in which ionization and curvature indicated the outgoing tracks were a π^- meson and a proton. Furthermore, events in which the outgoing tracks appeared to be π^- and π^+ were also found. Neither of these groups satisfied the elastic-scattering requirement that the incident and outgoing tracks be coplanar. These events may be interpreted as production of charged sigmas in which the Σ went backwards in the center of mass and had insufficient energy to leave a visible track, or else decayed so quickly after production that no track was visible. This hypothesis was tested by the computer programs for all two-prong events. In each case the incoming K^- and one of the outgoing tracks was used in fitting to the Σ-production hypothesis. Energy and momentum conservation require four constraints to be satisfied in the fit. Since the Σ is not seen, three of the constraining equations were used to calculate the Σ-production characteristics (its vector momentum, for example). This left the production fit with only one constraint. The Σ momentum so determined and the third observed track were fitted to the Σ-decay hypothesis. This fit is also once overdetermined, and was usually sufficient to identify the event. As a result, the invisible Σ's usually satisfied the following criteria. First, they would fail to fit either K^-p or π^-p elastic scattering; second, both the Σ production and subsequent Σ-decay hypotheses gave consistent fits with the data.

For those two-prong events where two final-state pions were observed, there were other possible interpretations. In addition to invisible $\Sigma^\pm$ hyperons, these events could also be charge-exchange reactions with very short $\bar{K}^0$ or $\Lambda\pi^+\pi^-$ production with a neutral decay of the Λ. Of the several hundred events initially in this $\pi^+\pi^-$ group, most proved to be resoluble kinematically into their four possible interpretations; the remainder were kinematically ambiguous. However, subsequent reexamination of the event on the scanning table frequently disclosed unmeasurably short but visible $\Sigma^\pm$ hyperons, or gaps corresponding to $\bar{K}^0$ mesons and in the proper direction to satisfy the kinematic fit obtained from the zero-length assumption. Those that did not yield to this re-examination were assigned to various categories according to their most probably interpretation. Fewer than 1% of them fell into this truly ambiguous class.

Another two-prong possibility arose from $\Sigma^+\rightarrow p\pi^0$ with a very small decay angle between the Σ^+ and proton. These generally came from energetic Σ^+ produced in the forward direction. Initially they were classified as two-prong events, but kinematic analysis and subsequent reexamination of these events showed them to be Σ^+.

One further effect should be mentioned. Any Σ^-

TABLE IV. Observed and predicted Σ^- absorptions for backward-produced Σ hyperons.

Momentum P_K (MeV/c)	Interval of $\cos\theta_{K^-\pi^+}$	Observed number of decays	Expected number of absorptions	Observed number of absorptions (visible Λ+invisible Λ)
293	1.0 to 0.9	4	5	3(3+0)
	0.9 to 0.8	11	2	0(0+0)
	0.8 to 0.7	14	0	2(2+0)
350	1.0 to 0.9	1	1	4(3+1)
	0.9 to 0.8	6	0	0(0+0)
390	1.0 to 0.9	17	10	8(3+5)
	0.9 to 0.8	24	0	3(3+0)
434	1.0 to 0.9	14	5	2(1+1)
	0.9 to 0.8	9	0	0(0+0)
513	1.0 to 0.9	9	1	2(1+1)
	0.9 to 0.8	6	0	0(0+0)
Totals			24(16+8)	24(16+8)

hyperon may interact with a proton according to

$$\Sigma^-+p\rightarrow\Sigma^0+n\rightarrow\Lambda+\gamma+n$$

or

$$\Sigma^-+p\rightarrow\Lambda+n.$$

The Λ would be visible only two-thirds of the time, when it would decay via its charged mode.

In order to estimate the number of Σ^- absorptions, the percentage of Σ^- hyperons that would stop and interact was calculated. The possibility of in-flight absorption was neglected. On the basis of the number of decays observed in any angular region, the corresponding number of absorptions may be estimated. Since the number of events considered is so small, large statistical fluctuations are not surprising. Table IV shows the comparison of observed and estimated absorptions. Although large fluctuations occur for the individual intervals, for the combination of all intervals agreement is quite satisfactory. Both the total number of absorptions and the division into visible and invisible Λ decay modes agree with the estimates extremely well.

Several checks can be made to verify that the effects of the biases seen above have been actually eliminated from our sample: (a) Figure 7 shows the distribution of observed times from production to decay compared with the known lifetimes. Agreement is very good. (b) The comparison of the pionic and protonic decay rates for the Σ^+ is shown in Table V. The over-all ratio of 0.51 agrees with the expected value of 0.51 ± 0.02.[1] (c) No significant depopulation or overpopulation near $\cos\theta_{K\pi}=1$ can be found in the Σ angular distributions (see Figs. 9 and 10) at any of the momentum intervals considered. This confirms the identification of the "zero-length" sigmas and justifies the confidence that no loss of such events has occurred.

Figure 8 shows the distribution of errors on the incident $-K^-$ momentum for $\Sigma^\pm$. Although there is a slight variation with production angle, the resolution seems sufficient to warrant division into 10-MeV/c intervals.

The angular distributions for each momentum setting are shown in Figs. 9 and 10. Again, a least-squares fit to powers of $\cos\theta$ was made to various orders. Tables VI and VII display the results of these fits. The curves drawn on Figs. 9 and 10 are the fits of order $n=2$. Since no corrections were needed, the observed numbers of events were used to calculate the $\Sigma^\pm$-production cross sections for each momentum exposure. These cross sections are shown in Tables VI and VII.

The polarization of the Σ^+ hyperon was observed through the up-down asymmetry of the protons in the decay $\Sigma_0^+\rightarrow p\pi^0$. The normal to the Σ production plane was defined by the unit vector $\hat{n}=\hat{K}_K\times\hat{K}_\pi/|\hat{K}_K\times\hat{K}_\pi|$,

TABLE V. Number of events and decay branching ratios of Σ^+ hyperons. The last two rows give the number of Σ^- and the Σ^+/Σ^- production ratios.

	Momentum (MeV/c)						
	293	350	387	392	434	513	Total
$\Sigma_0^+(\Sigma^+\rightarrow p+\pi^0)$	146	78	188	158	68	67	705
$\Sigma_+^+(\Sigma^+\rightarrow n+\pi^+)$	126	86	190	169	66	44	681
$\Sigma_0^++\Sigma_+^+$	272	164	378	327	134	111	1386
$\Sigma_0^+/(\Sigma_+^++\Sigma_0^+)$	0.54	0.48	0.50	0.48	0.51	0.60	0.508
Σ^- (all kinds)	199	106	219	194	99	72	889
$(\Sigma_0^++\Sigma_+^+)/\Sigma^-$	1.37	1.55	1.73	1.69	1.35	1.54	1.56

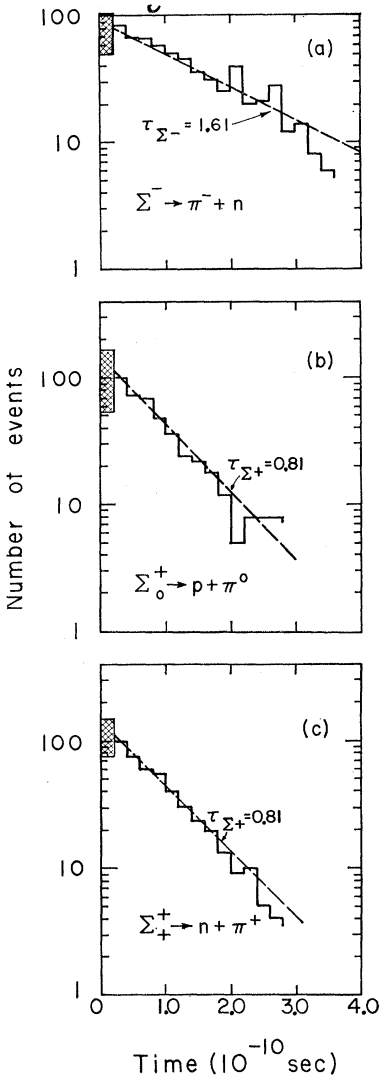

FIG. 7. Observed distribution of times from production to decay for Σ hyperons in the reactions (a) $K^-+p\rightarrow\Sigma^-+\pi^+$, $\Sigma^-\rightarrow\pi^-+n$; (b) $K^-+p\rightarrow\Sigma^+ +\pi^-$, $\Sigma^+\rightarrow p+\pi^0$; and (c) $K^-+p\rightarrow\Sigma^+ +\pi^-$, $\Sigma^+\rightarrow n+\pi^+$. The lines are drawn with a slope determined by the known lifetime (indicated on the graph in units of 10^{-10} sec); the vertical positioning is from an eye fit to the data. The shaded areas represent the two-prong events identified as Σ hyperons.

where $\hat{K}_K$ and $\hat{K}_\pi$ are unit vectors in the K^- and π^- directions. The angle β is the angle between $\hat{n}$ and the proton direction $\hat{q}_p$; $\cos\beta=\hat{q}_p\cdot\hat{n}$.

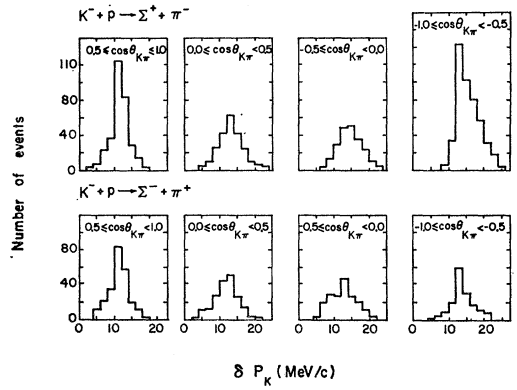

FIG. 8. Error in the incident-K^- fitted momentum for $\Sigma\pi$. The data are divided according to c.m. production angles; $\theta_{K\pi}$ is the angle between the incident K^- and the pion.

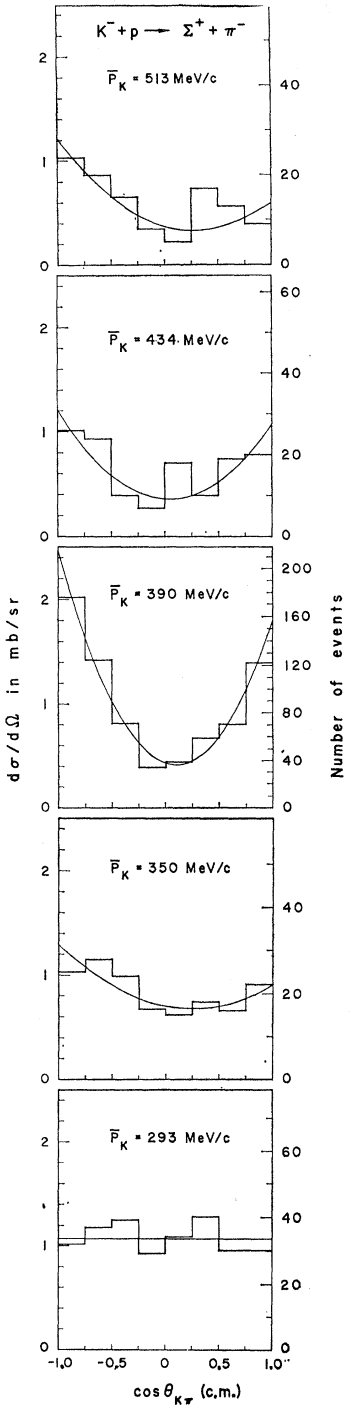

FIG. 9. Differential cross sections for the reaction $K^-+p\rightarrow\Sigma^+ +\pi^-$. The curves are best fits to the data.

The distribution of events versus θ (where $\sin\theta=\hat{K}_K\times\hat{K}_\pi$) and β becomes

$$\frac{d^2\sigma}{d\cos\theta d\cos\beta}=\pi I(\theta)[1+\alpha_0 P(\theta)\cos\beta], \qquad (1)$$

where $I(\theta)$ and $P(\theta)$ are the usual angular distribution and polarization functions of the production angle θ,

TABLE VI. Least-squares fits to the angular distributions for $\Sigma^+\pi^-$.

$\bar{P}_K$ (MeV/c)	σ (mb)	Order of fit	Expansion coefficients (mb/sr) C_0	C_1	C_2	C_3	C_4	χ^2	Expected χ^2	Confidence level (%)
293	13.6±1.4	0	1.07±0.06					3.8	7	80.3
		1	1.07±0.06	−0.06±0.11				3.1	6	79.6
		2	1.11±0.10	−0.06±0.11	−0.13±0.22			3.1	5	68.5
		3	1.11±0.10	−0.06±0.31	−0.13±0.22	0.00±0.49		3.1	4	54.1
		4	1.06±0.12	−0.08±0.31	0.50±0.90	0.02±0.49	−0.78±1.10	2.6	3	45.7
350	10.6±1.4	0	0.80±0.07					7.9	7	34.1
		1	0.82±0.07	−0.19±0.12				5.5	6	48.1
		2	0.70±0.09	−0.20±0.12	0.40±0.23			2.6	5	76.1
		3	0.71±0.10	−0.47±0.30	0.39±0.23	0.49±0.50		1.6	4	80.9
		4	0.66±0.12	−0.50±0.31	1.04±0.89	0.53±0.50	−0.84±1.11	1.0	3	80.1
390	12.5±0.8	0	0.75±0.03					173.9	7	$<10^{-5}$
		1	0.76±0.03	−0.21±0.07				165.5	6	$<10^{-5}$
		2	0.43±0.04	−0.35±0.07	1.70±0.14			6.6	5	25.2
		3	0.42±0.04	−0.22±0.16	1.71±0.14	−0.27±0.28		5.7	4	22.3
		4	0.40±0.05	−0.24±0.16	2.05±0.46	−0.24±0.29	−0.47±0.62	5.1	3	16.5
434	8.2±0.9	0	0.54±0.05					23.9	7	0.1
		1	0.54±0.05	−0.02±0.11				23.8	6	0.05
		2	0.35±0.07	−0.07±0.11	0.78±0.20			8.5	5	13.1
		3	0.36±0.07	0.13±0.23	0.78±0.20	−0.41±0.40		7.5	4	11.2
		4	0.33±0.09	0.12±0.23	1.21±0.77	−0.37±0.41	−0.57±0.97	7.2	3	6.6
513	7.5±1.1	0	0.47±0.05					23.3	7	0.2
		1	0.50±0.05	−0.22±0.10				18.6	6	0.4
		2	0.37±0.07	−0.31±0.11	0.53±0.18			9.8	5	8.1
		3	0.36±0.07	−0.03±0.27	0.59±0.18	−0.49±0.43		8.4	4	7.8
		4	0.27±0.08	−0.09±0.27	2.16±0.72	−0.36±0.43	−2.10±0.93	3.3	3	34.8

and α_0 is the decay-asymmetry parameter (helicity) in Σ_0^+ decay.[8] At an angle θ, the average value of $\cos\beta$ is given by

$$\langle\cos\beta\rangle_{\rm av}=\frac{\int\cos\beta[1+\alpha_0P(\theta)\cos\beta]d\cos\beta}{\int[1+\alpha_0P(\theta)\cos\beta]d\cos\beta}=\frac{\alpha_0P(\theta)}{3}. \quad (2)$$

The experimental quantity $\alpha_0P(\theta)$ and its uncertainty is then given for N events by

$$\alpha_0P(\theta)=\frac{3}{N}\sum_{i=1}^{N}\cos\beta_i\pm\left[\frac{3-(\alpha_0P)^2}{N}\right]^{1/2}. \quad (3)$$

D. Zero-Prong-Plus-V Events

Several interactions lead to the zero-prong-plus-V topology. Listed below are those energetically allowed at our momenta:

$$K^-+p\rightarrow\bar{K}^0+n \qquad \bar{K}^0\rightarrow K_1\rightarrow\pi^++\pi^- \quad (a)$$

$$\left.\begin{array}{l}\rightarrow\Lambda+\pi^0 \quad (b)\\ \rightarrow\Lambda+\pi^0+\pi^0 \quad (c)\end{array}\right\}\Lambda\rightarrow p+\pi^-$$

$$\left.\begin{array}{l}\rightarrow\Sigma^0+\pi^0 \quad (d)\\ \rightarrow\Sigma^0+\pi^0+\pi^0 \quad (e)\end{array}\right\}\Sigma^0\rightarrow\Lambda+\gamma,\quad\Lambda\rightarrow p+\pi^-.$$

[8] E. F. Beall, B. Cork, D. Keefe, P. G. Murphy, and W. A. Wenzel, Phys. Rev. Letters **1**, 285 (1961).

The $\Sigma^0\pi^0\pi^0$ cross sections are so small at the energies considered that these reactions were completely neglected.

Although each of these interactions leads to the same topological appearance, the $\bar{K}^0n$ events may be easily identified at the scanning table. The π^+ produced in the decay can be distinguished from the proton of a Λ decay because of its lighter ionization. In addition, the kinematical fit to the production and decay sequence described by (a) was also sufficient to identify the event unambiguously. (Very short $\bar{K}^0$ mesons, initially classified as two prongs, were subsequently identified by ionization and kinematics.) The $\bar{K}^0$ direction and $\pi^\pm$ momenta result in accurate values for the fitted incident K^- momentum. The average fitted K^- momentum error was 4 MeV/c. In order to obtain detailed cross sections, events from all runs were merged together to construct an ideogram of events versus K^- momentum. A computer program was employed which assigned to each event a unit area under a Gaussian curve centered at the fitted momentum and whose width was the fitted error. By this procedure the cross sections to be shown later were calculated in 10- and 20-MeV/c intervals over the resonance region. No finer division was made, since only a limited number of events was available. The average cross section for each of the beam-momentum exposures is displayed in Table II. To account for the invisible decay modes of K^0, the number of events was multiplied by 3 when cross sections were computed. Differential cross sections are given for each momentum run in

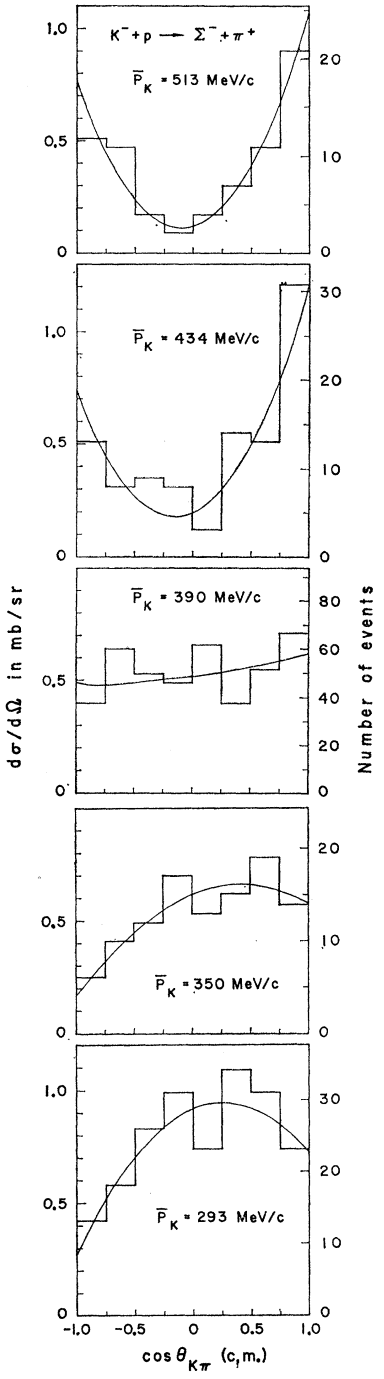

FIG. 10. Differential cross section for the reaction $K^- + p \rightarrow \Sigma^- + \pi^+$. The curves are best fits to the data.

Fig. 11. The 390-MeV/c data are shown fitted satisfactorily through $\cos^2\theta$.

Although the charge-exchange reactions discussed above were not difficult to identify, analysis of the reactions involving a Λ was less straightforward because, after identification of the Λ decay, no production fit is possible except for reaction (b). Even in the latter case, a fit would not help much in disentangling the direct lambdas of reaction (b) from the decay products of reaction (d).

The method followed was based on the "missing-mass" distribution. First, only those events were chosen in which the incident K^- momentum as measured by curvature was not different from the known beam momentum (as measured from τ decays) by more than 1.5 standard deviations. Those accepted were then averaged with their appropriate central beam momentum to obtain a better measure of the K^- momentum at the interaction point. This averaged momentum was then used

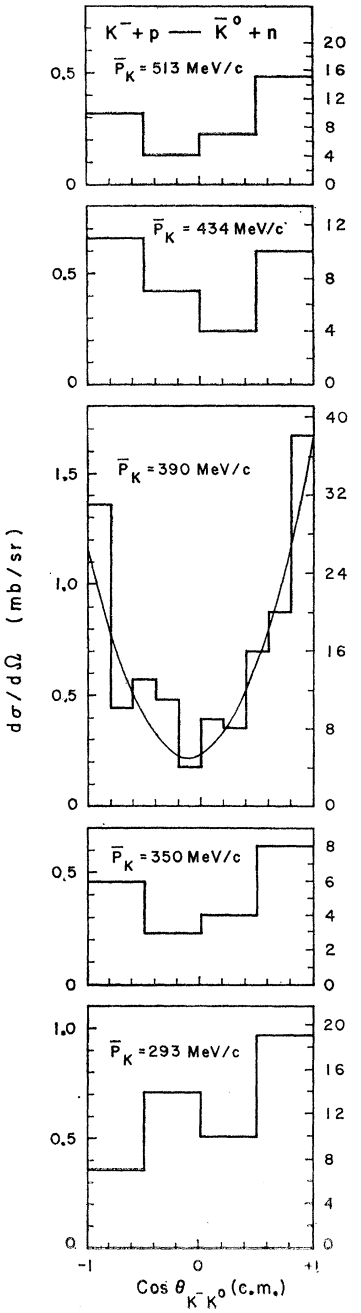

FIG. 11. Differential cross sections for the reactions $K^- + p \rightarrow \bar{K}^0 + n$; $\theta_{K^-\bar{K}^0}$ is the c.m. angle between the incident K^- and the $\bar{K}^0$. Because of the limited statistics no fit is shown except for the 390-MeV/c interval.

to transform the Λ momentum into the center mass of the K^-p system and to compute the total missing mass, μ, required to conserve four-momentum:

$$\mu^2=(E_{\text{c.m.}}-E_\Lambda)^2-P_\Lambda^2, \tag{5}$$

where $E_{\text{c.m.}}$ is the total center-of-mass energy and E_Λ and P_Λ are the Λ total energy and momentum in the c.m. system. Once the selected events were separated, the entire sample was divided in the same relative fraction.

Figure 12 shows the distribution of μ^2 at each momentum interval, along with the allowed limits for each type of interaction. Because of measurement errors, occasionally one finds $\mu^2<0$. Events giving $\mu^2<0$ are not shown on the graphs, but were added to the $\Lambda\pi^0$ portion when the relative fractions were determined. The graphs shown are ideograms. This is a convenient form for subdividing the events among the various possibilities; events with the same μ^2 value may have very different errors depending on their particular configuration. The effect of severe statistical fluctuations is also reduced.

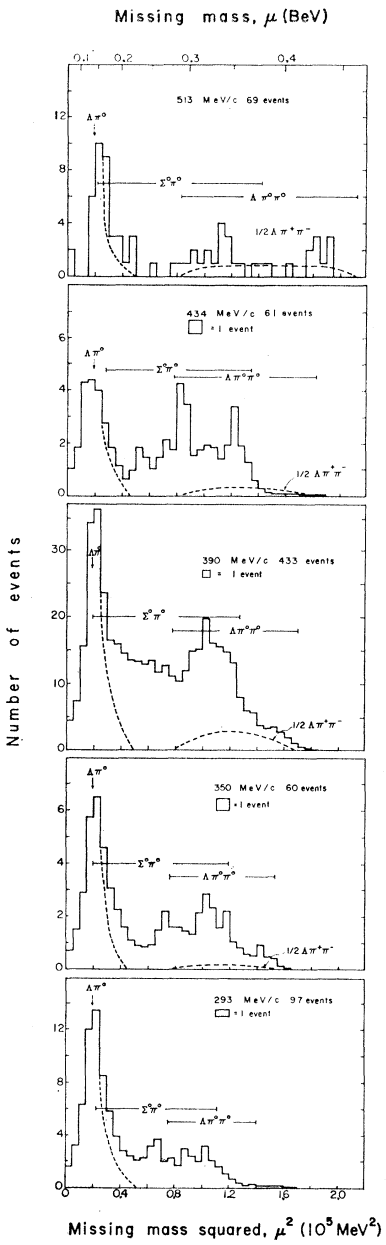

FIG. 12. Ideograms of the square of the missing mass, μ^2, from the reaction $K^-+p\rightarrow\Lambda+$neutrals (μ) at the various momentum exposures. Phase-space limits are drawn for the possible reactions.

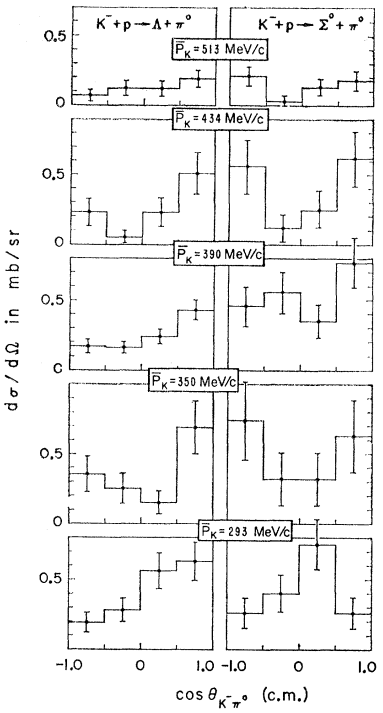

FIG. 13. Differential cross sections for the reactions $K^-+p\rightarrow\Lambda+\pi^0$ and $K^-+p\rightarrow\Sigma^0+\pi^0$. For the $\Sigma^0\pi^0$ events the Σ^0 is assumed to go in the Λ direction in the K^-p center of mass. Errors indicated are statistical.

For the $\Lambda\pi^0$ channel, μ^2 is uniquely the square of the π^0 mass. These events produce a peak centered around $(m_{\pi^0})^2$ with a roughly Gaussian distribution due to measurement errors. For the $\Lambda\pi^0\pi^0$ events, μ^2 is a distribution which begins at $(2m_{\pi^0})^2$, where the pions are at rest relative to each other, and extends up to a maximum value determined by the total energy available. For the $\Sigma^0\pi^0$ events, μ^2 also has a continuous distribution. The measured V is the Λ resulting from the decay of the $\Sigma^0(\Sigma^0\rightarrow\Lambda+\gamma)$. Here μ^2 varies because the Λ has different momentum and energy depending on the angle of its decay relative to the Σ^0 direction. The shape of the $\Lambda\pi^0\pi^0$ spectrum might be expected to follow phase-space predictions. The $\Sigma^0\pi^0$ spectrum can be shown to be rectangular, the uniform density being guaranteed by the isotropy of the Σ^0 decay angular distribution.

The $\Lambda\pi^0$ peak may be reconstructed on the high side by requiring symmetry with the low side. The dashed curve drawn over the peaks indicates the right side of the area assigned to the $\Lambda\pi^0$ fraction. At this stage the spectra have been separated into a pure $I=1$ part ($\Lambda\pi^0$) and pure $I=0$ part ($\Sigma^0\pi^0$ and $\Lambda\pi^0\pi^0$). The values of the $\Lambda\pi^0$ cross sections obtained at each momentum interval are shown in Table II. No subdivision into finer intervals

TABLE VII. Least-squares fits to the angular distributions for $\Sigma^-\pi^+$.

$\bar{P}_K$ (MeV/c)	σ (mb)	Order of fit	Expansion coefficients (mb/sr) C_0	C_1	C_2	C_3	C_4	χ^2	Expected χ^2	Confidence level (%)
293	10.0±1.1	0	0.73±0.05					17.1	7	1.7
		1	0.76±0.05	0.25±0.09				8.8	6	18.5
		2	0.92±0.09	0.22±0.09	−0.43±0.18			3.4	5	63.9
		3	0.92±0.09	0.28±0.27	−0.43±0.18	−0.11±0.40		3.3	4	50.9
		4	0.88±0.12	0.32±0.27	0.03±0.79	−0.15±0.41	−0.56±0.94	2.9	3	40.7
350	6.9±1.0	0	0.48±0.05					11.4	7	13.9
		1	0.52±0.05	0.23±0.08				3.6	6	73.1
		2	0.62±0.08	0.20±0.09	−0.24±0.17			1.6	5	90.1
		3	0.61±0.08	0.18±0.24	−0.24±0.17	0.04±0.37		1.6	4	80.9
		4	0.58±0.11	0.20±0.25	0.11±0.76	0.00±0.38	−0.42±0.90	1.4	3	70.6
390	6.9±0.5	0	0.52±0.03					15.7	7	2.5
		1	0.53±0.03	0.06±0.05				13.9	6	3.0
		2	0.52±0.04	0.07±0.05	0.02±0.10			13.9	5	1.6
		3	0.52±0.04	−0.22±0.12	0.06±0.10	0.51±0.20		7.2	4	12.6
		4	0.51±0.05	−0.22±0.12	0.12±0.39	0.51±0.20	−0.07±0.47	7.2	3	6.6
434	6.1±0.7	0	0.33±0.04					31.8	7	0.004
		1	0.34±0.04	0.10±0.09				30.5	6	0.003
		2	0.18±0.05	0.23±0.09	0.78±0.17			9.3	5	9.8
		3	0.18±0.05	−0.08±0.20	0.82±0.17	0.63±0.37		6.4	4	17.1
		4	0.20±0.06	−0.10±0.21	0.61±0.56	0.67±0.38	0.29±0.76	6.2	3	10.2
513	4.9±0.8	0	0.24±0.03					28.1	7	0.02
		1	0.25±0.03	0.10±0.09				26.7	6	0.01
		2	0.12±0.04	0.15±0.09	0.80±0.16			1.6	5	90.1
		3	0.11±0.04	0.10±0.18	0.81±0.06	0.11±0.34		1.6	4	80.9
		4	0.10±0.05	0.11±0.18	1.10±0.05	0.09±0.34	−0.36±0.74	1.3	3	72.9

is possible in this case because of the large uncertainty associated with the unfitted K^- momentum.

Further separation of the two $I=0$ reactions is more uncertain, since the spectra overlap considerably. The $\Lambda\pi^0\pi^0$ distribution extends beyond the $\Sigma^0\pi^0$ distribution, which provides a means for this division. If the $\Lambda\pi^0\pi^0$ events are distributed according to phase-space predictions, such a curve may be normalized to those events beyond the $\Sigma^0\pi^0$ limit. All remaining events are then attributed to the $\Sigma^0\pi^0$ channel.

At each momentum interval, the $\Lambda\pi^0\pi^0$ cross sections obtained in this way appeared to violate charge independence when compared with the $\Lambda\pi^+\pi^-$ cross sections. For $\Lambda\pi\pi$ production from the $I=0$ state, the ratio of the $\Lambda\pi^0\pi^0$ to $\Lambda\pi^+\pi^-$ is $\frac{1}{2}$. From the $I=1$ state, only $\Lambda\pi^+\pi^-$ can be made. Thus, the maximum allowable cross section for $\Lambda\pi^0\pi^0$ is one-half the $\Lambda\pi^+\pi^-$ cross section. This limit is represented on the spectra of Fig. 12 by the dashed curves labeled $\frac{1}{2}\Lambda\pi^+\pi^-$. The values obtained for the $\Lambda\pi^0\pi^0$ cross sections are shown in Table II where also the $\Lambda\pi^+\pi^-$ cross sections can be seen. This violation can probably be attributed to a relatively few poorly measured $\Sigma^0\pi^0$ events which fall beyond the $\Sigma^0\pi^0$ limit and are, thus, misidentified as $\Lambda\pi^0\pi^0$. Nevertheless, the persistence of the violation at all momenta indicates that the $\Lambda\pi\pi$ channel proceeds predominantly through the $I=0$ state. In order to better estimate the $\Sigma^0\pi^0$ cross section, the $\Lambda\pi^0\pi^0$ cross section subtracted was assumed in all cases to be $\frac{1}{2}\sigma(\Lambda\pi^+\pi^-)$. The values are shown in Table II. Here, again, no finer momentum subdivision is possible.

Since neither the Σ^0 nor the π^0 are seen directly or indirectly in the $\Sigma^0\pi^0$ channel, angular distribution and polarization are considerably less reliable than in the other channels. The Σ^0 has a typical momentum of 265 MeV/c in the K^-p center of mass. Hence, the Λ resulting from the decay may be expected to deviate from the Σ^0 direction by at most 15 deg. In all the angular distributions and polarizations recorded for $\Sigma^0\pi^0$, we assume that the Σ^0 and Λ directions are identical. However, unless we are dealing with a very complicated angular distribution involving many partial waves, the smearing effect is small relative to the statistical uncertainty. The polarization of the Σ^0 is deduced from the Λ polarization. The relationship is $\alpha_\Lambda P_\Lambda = -(1/3)\alpha_\Lambda P_{\Sigma^0}$. The angular distributions for $\Sigma^0\pi^0$ and $\Lambda\pi^0$ are shown in Fig. 13.

E. Two-Prong-Plus-V Events

For these events ($K^-+p\rightarrow\Lambda+\pi^++\pi^-$; $\Lambda\rightarrow p+\pi^-$), all tracks are measurable directly—such as the π^+ and π^-—or indirectly—like the Λ; thus the computer fit for each event is subject to four constraints. The average error on the K^- fitted momentum is 7 MeV/c. The first line of Table VIII shows the average cross section for each of the beam momentum settings. To obtain the cross sections in 10-MeV/c intervals, all events were fed into the Gaussian error ideogram routine also used

TABLE VIII. Cross sections for $\Lambda\pi^+\pi^-$ from visible and invisible Λ-decay events.

Momentum (MeV/c)	Cross section (mb) $\frac{3}{2}[\sigma(\Lambda\pi^+\pi^-, \Lambda \to p\pi^-)]$	$3[\sigma(\Lambda\pi^+\pi^-, \Lambda \to n\pi^0)]$
293	0.15±0.10	
350	0.9 ±0.3	0.9±0.3
390	1.6 ±0.2	1.3±0.2
434	1.5 ±0.4	0.7±0.3
513	2.0 ±0.4	1.9±0.5

for the $\bar{K}^0 n$ events. A factor of $\frac{3}{2}$ was used to account for the neutral decay mode of the Λ.

For each two $\Lambda\pi^+\pi^-$ events observed, there should be one event in which the Λ decays via the neutral mode and is not seen. Such events are two prongs. All two prongs were subjected to this hypothesis during the fitting procedure. Since both final-state tracks are pions, candidates for these events may easily be separated from K^-p and π^-p scatterings. Table VIII also shows the cross sections obtained from those events in which the

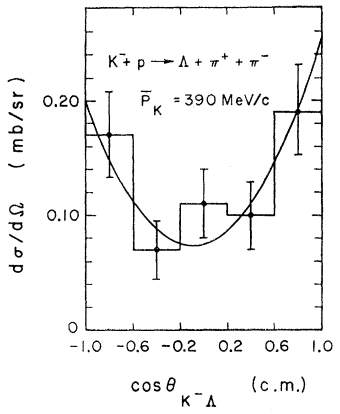

FIG. 14. Differential cross section for the reaction $K^-+p \to \Lambda+\pi^++\pi^-$ at 390 MeV/c. The angle is that between the incident K^- and the Λ. The curve shows a least-squares fit.

Λ decay was not seen. The consistency of the two cross sections is quite good.

Figure 14 shows the angular distribution of the Λ in the K^-p center of mass. The data are consistent with $1+3\cos^2\theta$ expected from a $J=\frac{3}{2}$ angular distribution if the dipion is assumed to be in the S state.

Figure 15 is a Dalitz plot of events in the 390-MeV/c runs. The other intervals have too few events to show any effect that might be present. If the distribution of pion energies were to follow phase space, this plot would be isotropic. The points are certainly consistent with this hypothesis. In addition to the Dalitz plot, the projections of the events on the two axes are shown in the same figure; the c.m. kinetic energy of each pion is divided by the total energy available, Q, to eliminate the effects of the incident-momentum spread. The threshold for $Y_1^*(1385)+\pi$ production is 405 MeV/c. Because of the width ($\Gamma \approx 50$ MeV) of Y_1^*, this threshold is diffuse and extends over more than 100 MeV/c. Production of Y_1^* would appear as broad bands parallel to the axes

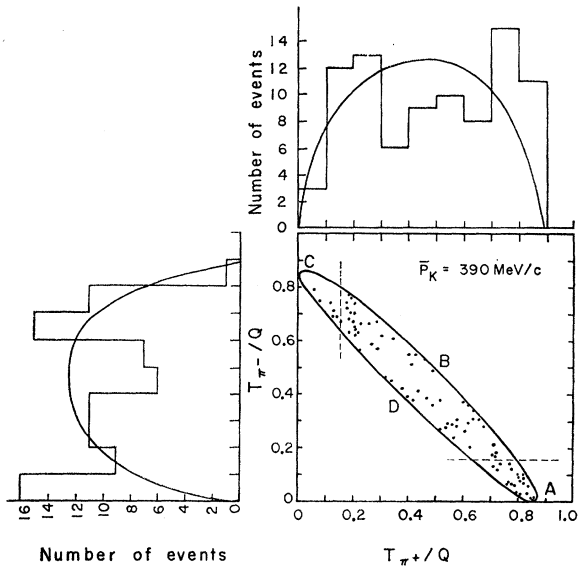

FIG. 15. Dalitz plot and projections for 87 reactions $K^-+p \to \Lambda+\pi^++\pi^-$, from the combined 387- and 392-MeV/c runs. Here Q is the total available kinetic energy in the K^-p center of mass. The curves on the plots represent phase space. Points A and C mark the vicinity where Y_1^* (1385) production would occur, with the dashed lines corresponding to Y_1^* of mass a half-width below 1385. At points D and B the Λ c.m. kinetic energy is maximum and minimum, respectively.

and centered outside of the phase-space curve, extending into the plot in the regions A and C. The lines indicate a mass $\frac{1}{2}\Gamma$ below the Y_1^* mass. An enhancement is suggested at A, but the data neither prohibit nor demand Y_1^* production.

A diagonal projection of the Dalitz plot on a 45-deg line, or equivalently a plot of the c.m. kinetic energy of the Λ, would display any $\pi\pi$ correlations. This is shown in Fig. 16. Although it is tempting to dismiss this distribution as being in accord with phase space, the situation is perhaps somewhat more involved. As discussed later, the $\Lambda\pi\pi$ channel proceeds largely from the K^-p, $I=0$, $D_{3/2}$ state. Since the $I=0$ state is symmetric, Bose statistics require the $\pi\pi$ system to be in an S or D state. Energetics favor the S state since the maximum di-pion relative momentum is 150 MeV/c. In either case, for negative $KN\Lambda$ parity, the Λ must be in a P orbital state relative to the dipion. Consequently, a P-wave centrifugal barrier should suppress low energy Λ. This

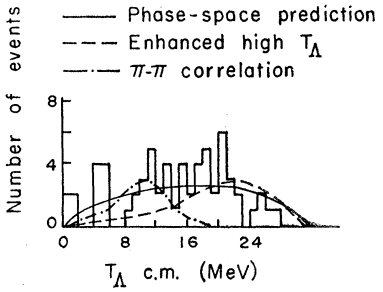

FIG. 16. Distribution of the Λ c.m. kinetic energy for 87 $K^-+p \to \Lambda+\pi^++\pi^-$ reactions, from the combined 387 and 392 MeV/c runs. Various distribution shapes are drawn.

is not observed. On the other hand, recent evidence from other experiments suggest a strong dipion effect in $I=0$ in the vicinity of $M_{\pi\pi}=400$ MeV.[9] This would tend to populate the region of low-kinetic-energy Λ hyperons and obscure the centrifugal-barrier effect. The net result experimentally is a phase-space-like distribution. This justifies the use of a phase-space curve in the $\Sigma^0\pi^0-\Lambda\pi^0\pi^0$ separation.

V. IDENTIFICATION OF THE RESONANCE

A. The 390-MeV/c Anomaly

It is clear from the data contained in the graphs of the previous sections and from Table II that there is a marked deviation in the behavior of the K^-p interaction in the vicinity of 390 MeV/c which disappears rapidly below and above this momentum. Significant enhancements are found in the $\bar{K}^0n$, $\Lambda\pi^+\pi^-$, $\Sigma^+\pi^-$, and $\Sigma^-\pi^+$ cross sections. Even more striking variations are seen in the angular distributions in most channels. The presence of a large $\cos^2\theta$ term in the K^-p channel at 400 MeV/c was observed in earlier experiments and reported by Alvarez and by Nordin.[2] Capps has conjectured that this arises from a K^-p interaction in the $D_{3/2}$ state.[10]

Using the large amount of data around this anomalous region, we have been able to explain the phenomena in terms of a resonance of the Breit-Wigner form occurring in a pure state of isotopic spin, angular momentum, and parity; in what follows we shall describe how this resonance, interfering with well-behaved nonresonant backgrounds, gives a very satisfactory fit to all the data. Confirmatory evidence for the existence of a resonance of this mass, width, and isotopic spin has been found in recent experiments involving three-body processes at higher K^-p and π^-p energies.[11] These experiments also agree roughly with our branching ratios, but yield no information on the phase of the resonant amplitude nor on the spin and parity of the resonant state.

In this section and in Sec. VI we shall discuss the identification of the quantum numbers and other characteristic properties of this state in a simplified way, leaving to Sec. VII a discussion of the least-squares computer fit to the data. This discussion will parallel closely the preliminary account published earlier,[3] with occasional differences in notation.

B. Resonance Theory—Elementary Remarks

There are several simple properties of a resonance which follow directly from the assumption that they are of the Breit-Wigner form and which are of great value in fixing the characteristic parameters of the resonance without recourse to an elaborate computer fit.

The resonant cross sections for elastic scattering and reactions are written as[12]

$$\sigma_e=\pi\lambda^2(J+\tfrac{1}{2})\frac{\Gamma_e^2}{(E_R-E)^2+\Gamma^2/4}, \tag{6}$$

$$\sigma_r=\pi\lambda^2(J+\tfrac{1}{2})\frac{\Gamma_e\Gamma_r}{(E_R-E)^2+\Gamma^2/4}, \tag{7}$$

where J is the total angular momentum of the resonant state; Γ_e, Γ_r, and Γ are the elastic, reaction, and total decay rates of the resonant state; $\Gamma=\Gamma_e+\Gamma_r$; E is the center-of-mass total energy; and E_R is the resonant energy. Clebsch-Gordan coefficients appropriate to the isotopic spin state will be introduced later. If there are several reaction channels, Γ_r may be further subdivided among these various channels. The Γ are not constants, but have an energy dependence that varies slowly over the region of the resonance and which, for the moment, we shall disregard.

Equations (6) and (7), expressing a resonant cross section behavior, are those appropriate to describe the phenomenological properties of an excited hyperon (Y^*). We may visualize the process of Y^* formation and decay as illustrated in Fig. 17. The K^-p system comes together to produce a metastable state which then decays either back into K^-p or into any of the other possible final states. The probability of formation of Y^* is proportional to its coupling to the incident K^-p channel. The probability of Y^* decay into any channel is proportional to that channel width. Hence, the cross section in any channel α will be proportional to the product $\Gamma_e\Gamma_\alpha$, leading to $\sigma_e\propto\Gamma_e^2$, $\sigma_r\propto\Gamma_e\Gamma_r$, as in Eqs. (6) and (7). For convenience, let us introduce the notation $\epsilon=(2/\Gamma)(E_R-E)$ and $x=\Gamma_e/\Gamma$, where ϵ is the number of half-widths removed from the resonant energy, and x, which we shall call the elasticity of the resonance, is the branching fraction into the elastic channel which plays an important role in its identification. With $\Gamma_r/\Gamma=1-x$, the equations may be written

$$\sigma_e=4\pi\lambda^2(J+\tfrac{1}{2})\frac{x^2}{\epsilon^2+1} \tag{6'}$$

and

$$\sigma_r=4\pi\lambda^2(J+\tfrac{1}{2})\frac{x(1-x)}{\epsilon^2+1}. \tag{7'}$$

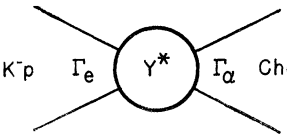

FIG. 17. Formation and decay of the Y^*.

[9] N. P. Samios, A. H. Bachman, R. N. Lea, T. E. Kalogeropoulos, and W. D. Shephard, Phys. Rev. Letters **9**, 139 (1962); C. Richardson, R. Kraemer, M. Meer, N. Nussbaum, A. Pevsner, R. Strand, T. Toohig, and M. Block, in *Proceedings of the 1962 International Conference on High Energy Physics at CERN* (CERN, Geneva, 1962); R. I. Kurz, Lawrence Radiation Laboratory Report UCRL-10564, 1962 (unpublished); J. Kirz, J. Schwartz, and R. Tripp, Phys. Rev. **130**, 2481 (1963).

[10] R. H. Capps, Phys. Rev. Letters **6**, 375 (1961).

[11] L. Bertanza *et al.*, W. A. Cooper *et al.*, J. Button-Shafer *et al.*, M. H. Alston *et al.*, G. Alexander *et al.*, and D. Colley *et al.*, in *Proceedings of the 1962 International Conference on High Energy Physics at CERN* (CERN, Geneva, 1962).

[12] J. M. Blatt and V. F. Weisskopf, *Theoretical Nuclear Physics* (John Wiley & Sons, Inc., New York, 1952).

The total cross section is $\sigma_T=4\pi\lambda^2(J+\frac{1}{2})[x/(\epsilon^2+1)]$. Notice that the ratio of the elastic cross section to the reaction cross section is independent of energy as long as Γ_e and Γ_r have the same energy dependence, and is simply $\sigma_e/\sigma_r=x/(1-x)$. For $\Gamma_e=\Gamma_r$, σ_r is maximum, so $x=\frac{1}{2}$ represents, in a sense, the condition for impedance match between the incident and the reaction channels.

For a simple two-channel resonance, the complex scattering amplitudes called the T matrix elements are given by

$$T=\frac{1}{\epsilon-i}\begin{pmatrix} x & [x(1-x)]^{1/2} \\ [x(1-x)]^{1/2} & 1-x \end{pmatrix}, \qquad (8)$$

with $\sigma=4\pi\lambda^2(J+1/2)|T|^2$.[13] For example, the diagonal elements may represent Kp and $\Sigma\pi$ elastic scattering, while the off-diagonal elements represent the processes $Kp\rightleftarrows\Sigma\pi$. All elements of T have the same energy dependence, $T\propto(\epsilon-i)^{-1}$. It is easily seen that this energy dependence requires that the T vector describe a circle in the complex plane, as illustrated in Fig. 18. Thus, all resonant scattering amplitudes pass through $\phi=\frac{1}{2}\pi$ at resonance. These properties of the Breit-Wigner resonance formula are not limited to a linear dependence of ϵ upon energy.

Let us consider now the general behavior of the elastic and reaction cross section in terms of the partial-wave amplitudes and connect them with the behavior of the Breit-Wigner amplitudes. An incident plane wave may be decomposed into incoming and outgoing spherical waves summed over all angular momenta. The nuclear interaction in a given partial wave alters only the outgoing wave, shifting it in phase and, if there is absorption, reducing it in amplitude. This is represented by a coefficient $\eta e^{2i\delta}$, where δ is a real phase shift and $\eta\leqslant 1$. In terms of these parameters the elastic cross section for each partial wave is given by[12]

$$\sigma_e=4\pi\lambda^2(J+\tfrac{1}{2})\left|\frac{\eta e^{2i\delta}-1}{2i}\right|^2, \qquad (9)$$

while the reaction cross section, obtained from conservation of probability (unitarity), is

$$\sigma_r=\pi\lambda^2(J+\tfrac{1}{2})(1-\eta^2). \qquad (10)$$

The relationships between η, δ and the elastic and reaction cross sections are illustrated in Fig. 19. The unitarity limits on σ_e and σ_r are given by the ordinate and the curves labeled $\delta=0$ and 90 deg.

Since for a resonance the ratio σ_e/σ_r is independent of energy, a resonance is depicted as a straight line of slope $x/(1-x)$. As a function of ϵ, one moves up the line, reaching the maximum at resonance where $\epsilon=0$ and then, beyond resonance, returns down the line. Notice that for an elasticity x greater than $\frac{1}{2}$, the elastic phase shift δ at resonance is $\frac{1}{2}\pi$, while for $x<\frac{1}{2}$ at resonance we have $\delta=0$. The latter condition exists for our resonance where $x=0.3$, which is shown as a dashed line in Fig. 19. One can understand this somewhat peculiar behavior of δ for $x<\frac{1}{2}$ by reference to Fig. 20.

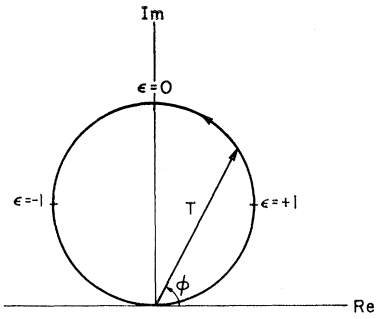

FIG. 18. The resonant T matrix amplitudes describe circles in the complex plane. Here we have $T\propto(\epsilon-i)^{-1}$ and $\tan\phi=\epsilon^{-1}$. The Wigner condition (Sec. VIB) requires that the circle be traversed counterclockwise as the energy increases.

It is important for the experimental identification of resonances by means of scattering processes such as the one considered here that the elasticity be not too small. If so the resonant effects may appear rather small, particularly in the elastic channel, since we have $\sigma_e\propto x^2$ and $\sigma_r\propto x$. This is especially true for strongly exothermic K^-p reactions at low energies, where a small bump may be obscured by a rapid $1/v$ falloff of the total cross section. However, although the elastic bump ($\propto x^2$) may be small and statistically not significant for small x, the elastic amplitudes will display interference effects in angular distributions which will be proportional to x and will, therefore, be more easily observed. This is the situation which prevails for the resonance discussed here.[14]

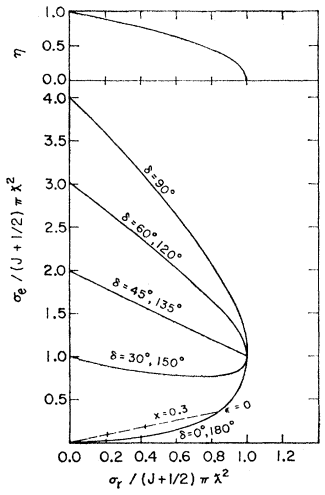

FIG. 19. Relationship between the elastic and reaction cross sections for a given partial wave. The region inside $\delta=0$ and 90 deg is allowed by unitarity. The line $x=0.3$ is the path followed by the resonance. The points $\epsilon=\pm1$ and ±2 are indicated by the vertical marks.

[13] For a discussion of the T and K matrices for multichannel strange-particle processes, see R. H. Dalitz, *Strong Interaction Physics and the Strange Particles* (Oxford University Press, New York, 1962).

[14] A higher-mass resonance, $Y_1^*(1660)$ [see L. W. Alvarez, M. H. Alston, M. Ferro-Luzzi, D. O. Huwe, G. R. Kalbfleisch, D. H. Miller, J. J. Murray, A. H. Rosenfeld, J. B. Shafer, F. T. Solmitz, and S. G. Wojcicki, Phys. Rev. Letters **10**, 184 (1963) and P. L. Bastien and J. P. Berge, Phys. Rev. Letters **10**, 188 (1963)], seems to have an even smaller $x\lesssim0.1$, which makes difficult its identification by means of scattering, whereas $Y_0^*(1815)$ [see O. Chamberlain, K. M. Crowe, D. Keefe, L. T. Kerth, A. Lemonick, Tin Maung, and T. F. Zipf, Phys. Rev. **125**, 1696 (1962)] has $x>\frac{1}{2}$ and was identified easily by total-cross-section measurements.

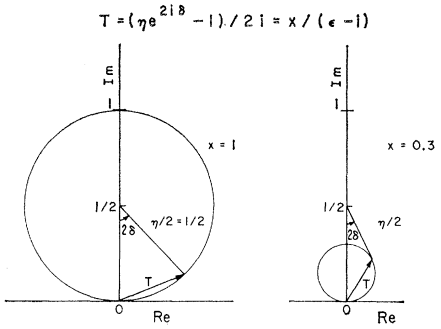

FIG. 20. Resonant scattering-amplitude circles given by $T=x/(\epsilon-i)$ for a purely elastic resonance ($x=1$) and for $Y_0^*(1520)$, where $x=0.3$. The amplitude T can also be expressed as $T=(\eta e^{2i\delta}-1)/2i$, where η and δ are as shown. When the resonance is purely elastic we have $\eta=1$, otherwise η depends on ϵ. For $x=1$ (or for any $x>\frac{1}{2}$), we have $\delta=\pi/2$ at resonance, while for $x<\frac{1}{2}$, δ reaches a maximum angle and then returns to zero at resonance. The phase of the resonant T amplitude, on the other hand, passes through $\pi/2$ for all cases. When expressed in terms of the eigenstate of the resonance (that linear combination of elastic and reaction states which is preserved through the interaction), one has by definition $x=1$, and the eigenstate phase shift always passes through $\pi/2$ at resonance. But, as noted above, in terms of the physical states this is only so for $x>\frac{1}{2}$.

C. Resonance Parameters

Further on, in Sec. VIII, we assemble the entire graphic account of the data as viewed by the computer. Figures 26, 27, 28, and 29 in that section show the cross sections for the various channels divided into finer momentum intervals to enable better study of the resonance. Several features of the resonance are immediately apparent from the behavior of the cross sections.

The *mass* of the resonance, taken as the c.m. energy corresponding to the momentum where the enhancements reach their maxima, is approximately 1520 MeV (394-MeV/c K^- laboratory momentum).

The resonance *width* Γ lies between 15 and 20 MeV (40 to 50 MeV/c).

No enhancement is noticeable in the $\Lambda\pi^0$ cross section (pure $I=1$); furthermore, roughly equal enhancements occur in the $\Sigma^+\pi^-$, $\Sigma^-\pi^+$, and $\Sigma^0\pi^0$ cross sections. This is precisely what one would expect if the *isotopic spin* of the resonance were equal to zero. [We assume charge independence; the Clebsch-Gordan coefficients for the various channels are given subsequently in Eq. (26).] Furthermore, experimental data show that we have $\Lambda\pi^0\pi^0/\Lambda\pi^+\pi^-\gtrsim\frac{1}{2}$ at resonance. This again supports a $I=0$ assignment since for $I=1(0)$ the ratio should be 0(1/2). One should note that in the reactions $K^-p\rightarrow\Lambda\pi^0$, $\Sigma^0\pi^0$, or $\Lambda\pi^0\pi^0$ which are topologically identical, a division of the reaction cross section into $I=1$ and $I=0$ can be achieved by separation of $\Lambda\pi^0$ ($I=1$) from $\Sigma^0\pi^0$ and $\Lambda\pi^0\pi^0$ (both $I=0$) without further subdivision of the latter two.

The *spin* of the resonant state can be deduced by inspection of the angular distribution at each momentum setting for the various channels by referring back to Figs. 6, 9, 10, 11, 13, and 14. A strong $\cos^2\theta$ term appears in all channels coupled to the resonance. This anisotropy is generally strongest at 390 MeV/c and usually disappears below and above the resonance. (The exception, $\Sigma^-\pi^+$, follows from the analysis, as will be seen later.) One is, therefore, led to the conclusion that the resonant state has a spin $J>\frac{1}{2}$. Furthermore, since analysis through $\cos^2\theta$ is generally sufficient to obtain a good fit, we conclude that the spin is most likely $\frac{3}{2}$. A value of $J=\frac{5}{2}$ would give rise to terms in the angular distribution up to $\cos^4\theta$. A further argument, based upon unitarity and discussed later, also favors $J=\frac{3}{2}$. A more quantitative evaluation of the resonance spin, containing both the angular distribution and unitarity requirements, is made in Sec. VII, where computer fits are discussed.

The assignment of $J=\frac{3}{2}$ allows two possibilities for the incident *orbital angular momentum* of the resonance: $P_{3/2}$ or $D_{3/2}$. The following argument strongly favors the latter case. Below 250 MeV/c, the K^-p interaction has been carefully studied in the S-wave zero-effective-range approximation.[1] It is found to within the accuracy of the experiments, that all cross sections and angular distributions agree very well with this approximation. The data at 293 MeV/c also agree with nearly pure S-wave interaction, while the 390-MeV/c angular distributions display a large amount of $\cos^2\theta$ with very little $\cos\theta$. The angular-distribution coefficients A_n, expressed in terms of the partial wave amplitudes S, P_1, P_3, D_3, and D_5, are found in Eq. (18). Inspection of these equations reveals that a $P_{3/2}$ resonance interfering with a dominant S-wave nonresonant interaction would result in large amounts of $\cos\theta$ appearing in the angular distribution; also the amount of $\cos^2\theta$ predicted in such channels as K^-p where the resonant component is fractionally small would be quite insignificant. On the other hand, a $D_{3/2}$ resonance leads naturally to the observed behavior. (We discuss this point more quantitatively in Sec. VD.) No $\cos\theta$ term results, since it requires interference between even- and odd-parity states.

The final resonance parameter to be fixed is x, the *elasticity* of the resonance given by $x=\Gamma_e/\Gamma$. The resonating part of the $\bar{K}^0n$ channel appears to be about

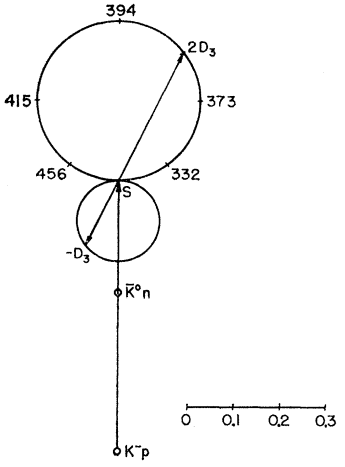

FIG. 21. The S and D_3 amplitudes for K^-p and $\bar{K}^0n$ in the vicinity of the resonance. The resonance is taken centered at 1520 MeV with a constant width $\Gamma=16$ MeV. Momenta (in MeV/c) are indicated on the periphery of the $2D_3$ circle. The imaginary axis is vertical and the amplitudes are dimensionless.

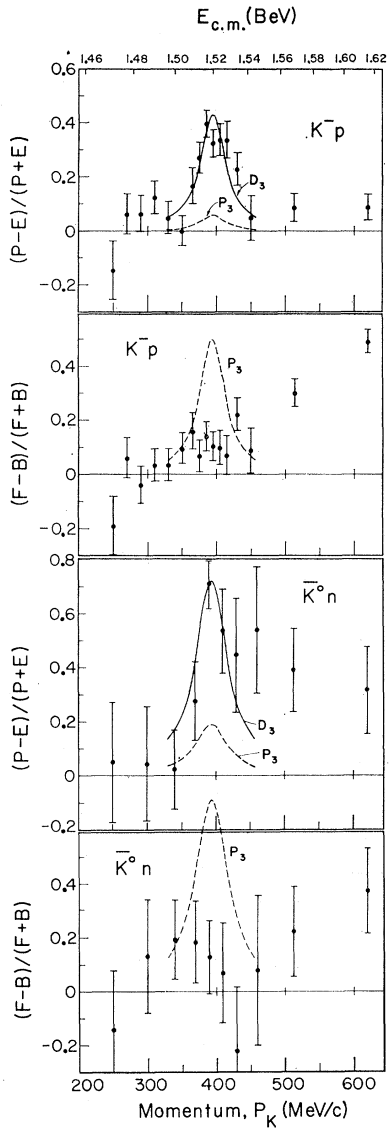

FIG. 22. The $(P-E)/(P+E)$ and $(F-B)/(F+B)$ data for K^-p and $\bar{K}^0n$ as a function of momentum. The solid curves correspond to a D_3 resonance as constructed from Fig 21. The dashed curves are calculated for a P_3 resonance.

5 mb on a 5-mb background. The K^-p channel also shows about a 5-mb enhancement on a 30- to 35-mb background. (With such a large nonresonant background, however, the statistical significance of the enhancement is largely obscured.) Introducing the appropriate Clebsch-Gordan coefficient for a $I=0$ resonance into Eq. (6′), and taking $J=\frac{3}{2}$, one finds for the resonant state in the elastic channel $\sigma_{K^-p}=\sigma_{\bar{K}^0n}=2\pi\lambda^2x^2$. Since $\pi\lambda^2$ equals 20.8 mb at resonance, a 5-mb resonant cross section yields $x=0.35$. By inspection of Fig. 19 we see that for a value of x in this region, the elastic channel, compared to the reaction channel, is a very sensitive function of x (note that in the figure the ordinate and abscissa are to different scales). Thus, the elastic channel cross section, and, in particular, $\bar{K}^0n$ where the nonresonant background is small, gives an immediate and sensitive measure of x. The best computer fit to the data in all channels, including angular distributions, reduces this estimate to $x=0.29\pm0.03$ for a $J=\frac{3}{2}$ resonance.

The reaction channels available to an $I=0$ resonance are $\Sigma\pi$ and $\Lambda\pi\pi$. The $\Lambda\pi^+\pi^-$ enhancement is about 2.5 mb, leading to an enhancement of about 4 mb for $\Lambda\pi^+\pi^-+\Lambda\pi^0\pi^0$. The various $\Sigma\pi$ channels yield an enhancement of $5+3+4=12$ mb for $\Sigma^+\pi^-+\Sigma^-\pi^++\Sigma^0\pi^0$. These should all be equal if there is no $I=1$ background in the $D_{3/2}$ state. The experiment thus suggests that there is present some nonresonant $D_{3/2}I=1$ background. Another possibility is that charge independence is violated to some extent, due perhaps to mass differences in the various $\Sigma\pi$ charge states (this is discussed in Sec. IX). Using the over-all computer fit, the branching ratios for the resonant state become $\bar{K}N:\Sigma\pi:\Lambda\pi\pi=30:55:15$, where the symbols signify the sum of the rates into all charge states. The uncertainty on each number is about 5.

The value of $x=0.35$ obtained from the enhancement in the cross section predicts, through unitarity, a definite enhancement in the reaction cross section. With the inclusion of the Clebsch-Gordan coefficient, a $J=\frac{3}{2}$ resonance gives $\sigma_r=2\pi\lambda^2(J+\frac{1}{2})x(1-x)=19$ mb. The $J=\frac{5}{2}$ possibility would require, for the same size of the elastic bump, an enhancement of 25.4 mb. Since the enhancement appears experimentally to be approximately 16 ± 3 mb this can be considered as a fairly strong argument favoring $J=\frac{3}{2}$.

D. $K-p$ and $\bar{K}^0n$ Differential Cross Sections

In Sec. VC above, we have seen how nearly all the properties of the resonant state can be inferred from an

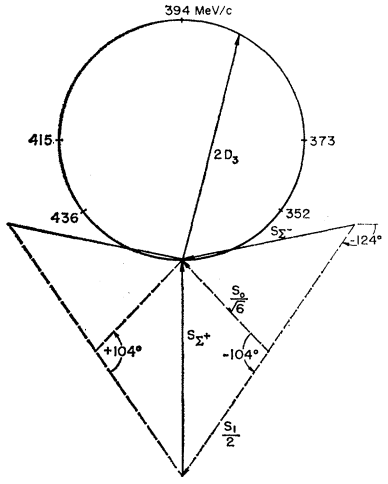

FIG. 23. Diagram showing the nonresonant S wave $\Sigma\pi$ amplitudes and the resonant $2D_3$ amplitude. The data demand that S_{Σ^+} and D_3 be in phase at resonance as shown in order to yield a large $\cos^2\theta$ in the angular distribution. This leaves two possible S_{Σ^-} directions as shown, differing in $\phi_{S_0-S_1}=\pm104$ deg. Since the Σ^- angular distribution goes from $\sin^2\theta$ below resonance to $\cos^2\theta$ above resonance, the right-hand orientation is correct. The angle $\phi_{S_1-D}=124$ deg. Momenta are indicated on the periphery of the $2D_3$ circle.

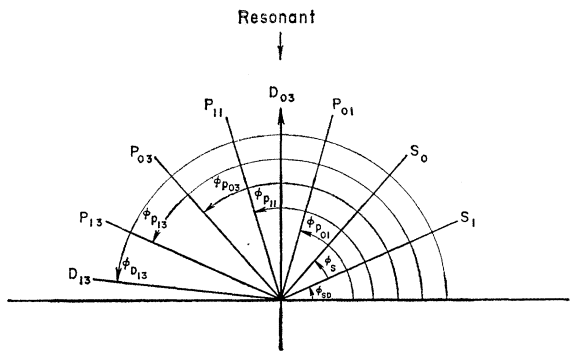

FIG. 24. Graphic definition of the phases used in the computer fit to the data. Note that, except for the S_0 amplitude, all nonresonant phases are defined relative to the real axis.

inspection of the behavior of the various partial cross sections plus the observation that only even powers of $\cos\theta$ appear strongly in the K^-p and $\bar{K}^0n$ angular distributions at resonance. Let us now investigate these angular distributions more quantitatively within the framework of a simple model.

Assume that the S-wave interaction is given by a constant scattering length A. The phase shift δ is then written $K\cot\delta=1/A$, where $K=1/\lambda\!\!\!^{-}$. Absorptive processes lead to a complex $A=a+ib$. The elastic-scattering amplitude for complex δ is $T_e=(e^{2i\delta}-1)/2i$, which can be written as $T_e=KA/(1-iKA)$. For low-energy K^-p interactions, b is found to be large, and because of this a becomes difficult to determine. This is especially true for the strongly absorptive $I=0$ where a for both Humphrey-Ross solutions is consistent with zero. Although an oversimplification, it is instructive to set $a=0$. Then we have $T_e=iKb/(1+Kb)$; thus, T_e is always imaginary. For $Kb\gtrless1$ we have $T_e\gtrless i/2$. From Fig. 20 this corresponds to the real phase shift $\delta=0$ or $\frac{1}{2}\pi$. Accordingly, the elastic and reaction cross sections as a function of momentum, follow the right-hand boundary of the region illustrated in Fig. 19.[15]

A predominantly imaginary scattering amplitude is also inferred from the optical theorem $\mathrm{Im}f(0)=(K/4\pi)\sigma_T$. Here $f(0)$ and σ_T are, respectively, the forward $K-p$ scattering amplitude and the total cross section. These are displayed on the right side of Fig. 6. To a fairly good approximation we may then take the S-wave amplitudes to be purely imaginary.

We can calculate the S-wave $\bar{K}N$ magnitudes from the experimental cross section data. From Eqs. (16) and (18) one obtains through $J=\frac{3}{2}$,

$$\sigma=\int Id\Omega=4\pi\lambda\!\!\!^{-2}[|S|^2+|P_1|^2+2|P_3|^2+2|D_3|^2].$$

Since the squares of the small P waves contribute negligibly to the cross section, we may disregard them in this approximate treatment. Subtracting the 5-mb enhancement coming from the resonant D_3 state we then obtain, using 30 mb and 5 mb for the nonresonant K^-p and $\bar{K}^0n$ cross sections, respectively, $S_{K^-p}=0.60i$, $S_{\bar{K}^0n}=0.25i$.[16] The momentum dependence of these amplitudes in the vicinity of the resonance is described quite satisfactorily by a constant complex scattering length. We also have $D_{K^-p}=D_{\bar{K}^0n}=0.175/(\epsilon-i)$.

The angular distribution resulting from S and D_3 waves is

$$I=\frac{1}{K^2}(|S+2D_3|^2\cos^2\theta+|S-D_3|^2\sin^2\theta). \quad (11)$$

Both S and D_3 amplitudes have already been fixed from the cross sections so the K^-p and $\bar{K}^0n$ angular distributions can be calculated and compared with the data. One can obtain the coefficients of $\cos^2\theta$ and $\sin^2\theta$ most simply by the graphical construction shown in Fig. 21. The circles represent the amplitudes $2D_3$ and $-D_3$, and the amplitudes S_{K^-p} and $S_{\bar{K}^0n}$ are vectors from the points labeled K^-p and $\bar{K}^0n$ to the point S. Since the resonance is narrow, let us for convenience fix the S amplitudes to be constant in the momentum range where the resonance is appreciable. One immediately sees that at resonance the S and D_3 waves interfere constructively to produce a large $\cos^2\theta$ and destructively to reduce the $\sin^2\theta$. Thus, a small enhancement in the cross section can alter the angular distribution in the striking way observed. Expressing the angular distribution in terms of the number of polar ($|\cos\theta|>0.5$), equatorial ($|\cos\theta|<0.5$), front ($\cos\theta>0$), and back ($\cos\theta<0$)

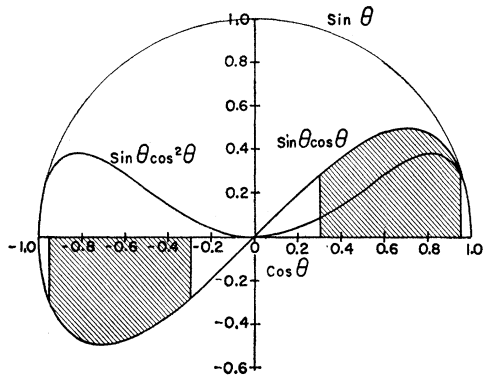

FIG. 25. Sinθ, sinθ cosθ, and sinθ cos$^2\theta$ plotted versus cosθ. The shaded area between $0.95\geq|\cos\theta|\geq0.30$ is the angular interval where sinθ cosθ is large and is the region used to obtain the average value of this polarization term.

[15] Note that for the Humphrey-Ross solution 1, we have $b\approx3$ F in $I=0$; so $Kb=1$ occurs at a very low momentum of about 100 MeV/c. Where we are situated Kb is $\gg1$; so σ_T approaches 0 and σ_e approaches $4\pi\lambda\!\!\!^{-2}$, i.e., the S wave appears always in "resonance" at higher energy. Of course, the scattering length will not remain constant, and nonzero values of a will also cause deviations from this simple behavior, but the data suggests that this picture is reasonably correct.

[16] In terms of isotopic-spin scattering lengths, these yield $b_0=4.6$ F and $b_1=0.44$ F. These may be compared with the Humphrey-Ross solutions in Table XII.

events—abbreviated P, E, F, and B—one can write

$$\frac{P-E}{P+E}=\frac{A_2}{4(A_0+\frac{1}{3}A_2)} \tag{12}$$

and

$$\frac{F-B}{F+B}=\frac{A_1}{2(A_0+\frac{1}{3}A_2)}, \tag{13}$$

where A_n are coefficients of $\cos^n\theta$ in the differential cross section. Figure 22 shows the K^-p and $\bar{K}^0n$ data compared with this simple calculation for a D_3 and also a P_3 resonance. The data clearly prefer a D_3 resonant $K-p$ state. The rising F–B ratio can be attributed to the gradual appearance of nonresonant P waves neglected in this calculation.

VI. $KN\Sigma$ PARITY

In this section we shall discuss the arguments that lead to the establishment of the Σ parity. Approximations to the experimental situation will occasionally be made so as not to obscure the simplicity of the reasoning with nonessential details. A more elaborate treatment of the problem will be found in Sec. VII dealing with the computer analysis.

In Sec. IV we have shown that the experimental data strongly favor an incident $K-p$ resonant D state, with the most likely angular momentum being $J=\frac{3}{2}$. With the parity of the incoming angular-momentum state identified, the determination of the Σ parity becomes a matter of measuring the orbital angular momentum of the $\Sigma\pi$ state; $D_{3/2}$ for negative $KN\Sigma$ parity, $P_{3/2}$ for positive $KN\Sigma$ parity.

We shall now consider the various ambiguities that may be present in the problem and how they can be resolved.

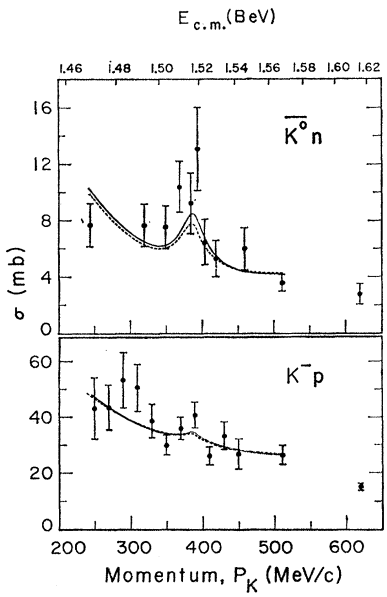

FIG. 26. Cross sections for K^-p charge exchange and elastic scattering as a function of momentum. The solid line corresponds to solution I for negative $KN\Sigma$ parity; the dashed line corresponds to solution V for positive $KN\Sigma$ parity. These two solutions are shown in Figs. 26 through 38. The only significant difference between them appears in connection with the polarization effects.

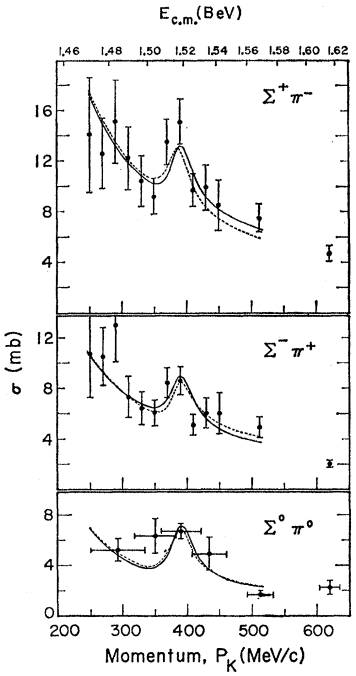

FIG. 27. Cross sections for $\Sigma^+\pi^-$, $\Sigma^-\pi^+$, $\Sigma^0\pi^0$ as a function of momentum.

A. The Minami Ambiguity

The simplest and least elegant way of seeing the Minami ambiguity is by direct inspection of Eqs. (18) and (19).[17] Restricting consideration to $J=\frac{1}{2}$ and $J=\frac{3}{2}$, we see that under an interchange of parity of each state, i.e., $S\rightleftarrows P_1$, $D_3\rightleftarrows P_3$, the coefficients A_n in I remain the same, while the coefficients B_n in IP change sign. Thus, all angular distributions remain invariant while polarizations change sign. This is a general statement valid for the parity interchange of all amplitudes through whatever J. Where new particles are produced in the final state, the Minami transformation can be carried out on the initial or the final state or both, leading to a fourfold ambiguity if only angular distributions are measured. The two-fold ambiguity involving the incoming $\bar{K}N$ state is, as we have seen, resolved by continuation of the $\bar{K}N$ amplitudes from the low-energy region, where they are known to be purely S wave, to the 400-MeV/c region. Thus, the $S\rightleftarrows P_1$ ambiguity is not present for the incoming state.

Since the $Kp\rightarrow\Sigma\pi$ reaction is exothermic (for K^-p at rest we have $P_\Sigma=180$ MeV/c), no argument analogous to the one for the incoming state can be constructed for the $\Sigma\pi$ state. Within the K-matrix formalism, differences do exist between S and P outgoing states, but the effects are not large and, furthermore, are subject to the assumption of constancy of the K-matrix elements.

[17] For other discussions of these ambiguities, see M. Nauenberg and A. Pais, Phys. Rev. 123, 1058 (1961). Yang-type ambiguities as applied to this problem are considered by R. H. Capps, Phys. Rev. 126, 1574 (1962).

The polarization in certain channels can, however, be measured, and this provides the means of resolving the remaining ambiguity. Beall *et al.*,[8] have measured the helicity α_0 of protons in the decay mode $\Sigma_0^+ \to p\pi^0$, and find it to be $\alpha_0 = -0.78_{+0.09}{}^{-0.08}$. Alpha is related to the asymmetry of the decay protons from polarized Σ hyperons by $I = 1 + \alpha \hat{q} \cdot \mathbf{P}_\Sigma$, where $\hat{q}$ is the direction of the decay *proton* in the Σ center-of-mass system and $\mathbf{P}_\Sigma$ is the Σ polarization. The decays $\Sigma_+{}^+ \to n\pi^+$ and $\Sigma^- \to n\pi^-$ are known to have small asymmetry parameters, so these events cannot be utilized as analyzers of Σ polarization. If one assumes the validity of the $\Delta T = \frac{1}{2}$ rule in Σ decays, then[18] $\alpha_0 = -1$; we shall assume $\alpha_0 = -1$ in our calculations. The Λ resulting from Σ^0 have a polarization given by $\mathbf{P}_\Lambda = -\frac{1}{3}\mathbf{P}_\Sigma$, and the subsequent decay $\Lambda \to p\pi^-$ has an asymmetry parameter $\alpha_\Lambda = +0.67_{-0.18}{}^{+0.24}$,[19] which is used in our calculations. The factor of 3 loss in polarization in Σ^0 decay coupled with previous mentioned problems associated with these events allows little more than a consistency check from the Σ^0 data. The crucial measurement is then the Σ^+ polarization from that half of the 1300 Σ^+ events which decay through the $\Sigma_0{}^+$ mode.

B. Complex-Conjugation Ambiguity: The Wigner Condition

Let us refer again to Eqs. (18) and (19) for the coefficients A_n, B_n and observe that if one takes the complex conjugate of each partial-wave amplitude, then the cross section is again invariant, while the polarization changes sign. This is an additional ambiguity; thus, it is not sufficient to measure the polarization in order to establish the parity. A further condition is needed in order to resolve the problem.

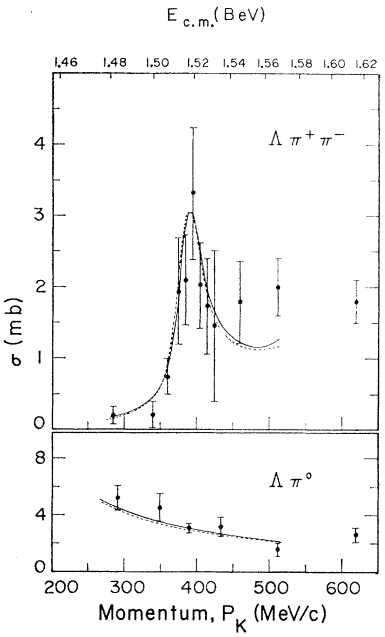

FIG. 28. Cross sections for $\Lambda\pi^+\pi^-$ and $\Lambda\pi^0$ as a function of momentum.

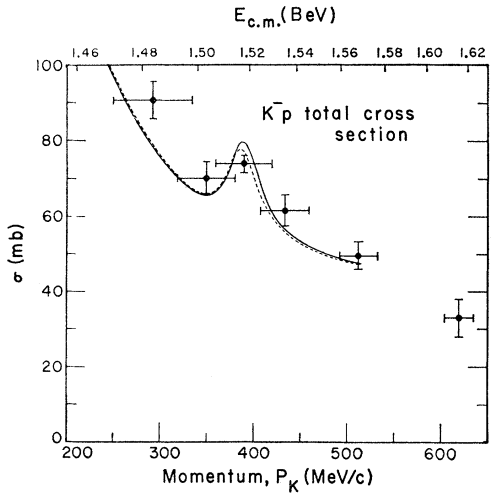

FIG. 29. The K^-p total cross section plotted as a function of momentum.

For the nonresonant amplitudes, there is no way of deciding whether an amplitude or its complex conjugate is to be chosen. However, for the resonant state, causality in the form of the Wigner condition prescribes the appropriate energy dependence of the resonant amplitude. Wigner[20] has shown that the amplitude of a narrow elastic resonance must as a function of energy, traverse the complex plane in a counterclockwise direction (see Fig. 18). His causality argument can be summarized as follows: Consider a wave packet resolved into its incoming and outgoing spherical waves and incident on a scattering center of radius R. The group velocity is given by $d\omega/dK$, where K is the wave number and ω is the frequency. The radial dependence of the incoming wave is then $r_i = -(d\omega/dK)t$. After scattering, the wave suffers a phase shift 2δ, and the outgoing radial dependence is given by $r_0 = +(d\omega/dK)t - 2d\delta/dK$. If the outgoing wave is not to leave the scattering region before the arrival of the incoming wave on the surface R, then for $r_i = R$ we must have $r_0 < R$. This yields the inequality $d\delta/dK > -R$. Hence, the phase shift cannot decrease with arbitrary rapidity as a function of energy. The width of the 1520 resonance gives a value of $d\delta/dK \approx 12\lambda\!\!\!^{-}_\pi$. The radius of interaction R would have to be larger than $12\lambda\!\!\!^{-}_\pi$ in order to have the resonant amplitude describing a clockwise circle and still satisfy the Wigner condition.[21] This result can be generalized for inelastic

[18] R. D. Tripp, M. B. Watson, and M. Ferro-Luzzi, Phys. Rev. Letters **9**, 66 (1962).

[19] E. Beall, B. Cork, D. Keefe, P. Murphy, and W. Wenzel, Phys. Rev. Letters **8**, 75 (1962). J. W. Cronin and O. E. Overseth, in *Proceedings of the 1962 International Conference on High-Energy Physics at CERN* (CERN, Geneva, 1962), have more recently determined α_Λ to be 0.62 ± 0.07.

[20] E. P. Wigner, Phys. Rev. **98**, 145 (1955).

[21] Slow decrease of amplitude through $\delta = \pi/2$ do occur in particle physics. A well-known example occurs in ${}^3S_1$ np scattering at about 15 MeV. Another case might perhaps occur in S wave K^+p scattering above 1 BeV/c. These, however, should not be con-

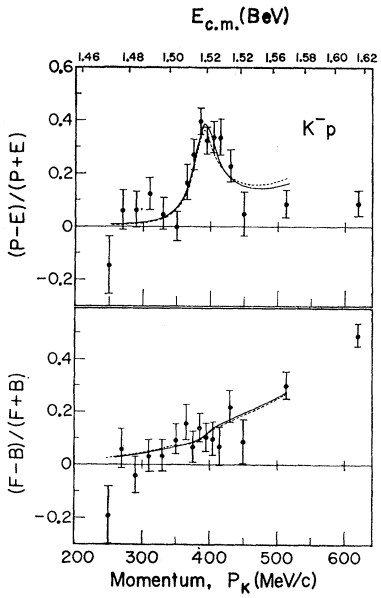

FIG. 30. Polar-equatorial and front-back ratios for K^-p scattering as a function of momentum:

$$\frac{P-E}{P+E}=\frac{A_2}{4(A_0+\frac{1}{3}A_2)};\quad \frac{F-B}{F+B}=\frac{A_1}{2(A_0+\frac{1}{3}A_2)}.$$

processes as well, and if we are dealing with a simple isolated resonance, as appears to be the case, then the result must still hold.[22] The ambiguity associated with complex conjugation is thereby removed.

C. Diagrammatic Analysis of the $\Sigma\pi$ Data

For the sake of fixing the notation during the subsequent discussion, we shall here assume that, as the data will show later, the $KN\Sigma$ parity is negative. The incident K^-p S state then feeds the $\Sigma\pi$ S state, etc. The discussion would follow similarly for the other parity assumption except for the final polarization argument.

The $\Sigma\pi$ partial cross-section data indicate a monotonic decrease with momentum characteristic of an exothermic reaction proceeding through the incident S wave. Superposed on this behavior there appears a sizeable enhancement in all three channels at the momentum corresponding to the 1520-MeV resonance. Thus, as in the incident channel, S waves appear to dominate the behavior, apart from the resonance. However, P waves are clearly evident through their interference with even parity states. This is seen in the significant $\cos\theta$ terms in the angular distributions and $\sin\theta$ term in polarization. Nevertheless, as the computer fits show, the S waves still play the dominant role. To fix them in the framework of charge independence one must determine the $T=0$ and $T=1$ magnitudes, S_0 and S_1, and their relative phase, $\phi_S=\phi_{S0}-\phi_{S1}$. These can be extracted from the charge-independence relationships:

$$\Sigma^{\pm}:\quad |S|^2=\tfrac{1}{6}|S_0|^2+\tfrac{1}{4}|S_1|^2\mp\frac{1}{\sqrt{6}}|S_0||S_1|\cos\phi_S$$

$$\Sigma^0:\quad |S|^2=\tfrac{1}{6}|S_0|^2.$$

Here S_0 is fixed by the nonresonant $\Sigma^0\pi^0$ cross section. Then S_1 can be obtained from the $\Sigma^+ + \Sigma^- - 2\Sigma^0$ nonresonant cross section and finally ϕ_S from the $\Sigma^+ - \Sigma^-$ nonresonant cross section. At low energy this phase angle is well determined from $K-p$ captures at rest to be $\phi_S=\pm 60$ deg and has been found to increase to about 90 deg at 250 MeV/c (with a discontinuity in the energy derivative theoretically predicted at the $\bar{K}^0n$ threshold). Our experiment indicates, from the behavior of the nonresonant Σ^+ and Σ^- cross sections, that this phase angle continues to increase with momentum, reaching about 105 deg at the resonance. Beyond this momentum, P waves become sufficiently large that its behavior from there on is uncertain. The best computer fit to the data yields, between 250 MeV/c and 513 MeV/c, an average angle $\phi_S=-104$ deg (the sign is discussed below). The S-wave $\Sigma\pi$ magnitudes at the resonance are given by the computer analysis to be $|S_0|=0.405$ and $|S_1|=0.405$.

The S-wave parameters are now fixed by the nonresonant cross sections with the exception of the over-all S-wave phase angle of the $\Sigma\pi$ channels. This can be determined by a study of the interference between the S amplitude and the resonant D_3 amplitude whose phase is fixed by its resonant form. The interference results in a $\cos^2\theta$ term in the angular distribution [(see Eq. (11)]. The Σ^+ reveals a large $\cos^2\theta$ at resonance fall-

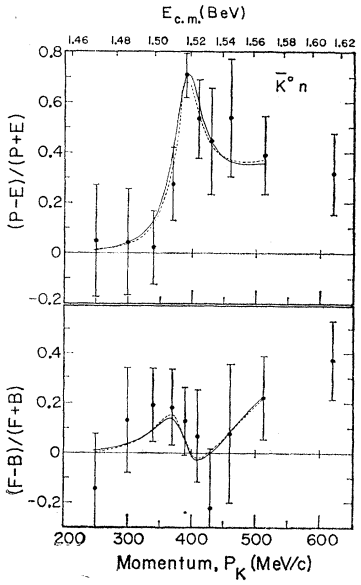

FIG. 31. Polar-equatorial and front-back ratios for $\bar{K}^0n$ scattering as a function of momentum.

sidered resonances in a strict sense. Typically they occur when a negative reciprocal scattering length is cancelled by a positive effective-range term.

[22] We are indebted to Professor R. H. Dalitz for a discussion concerning this point.

ing rapidly on both sides (Fig. 9). This implies that the S and D_3 amplitudes must be approximately in phase at resonance for the $\Sigma^+\pi^-$ channel, as illustrated in Fig. 23. The S-wave amplitude for $\Sigma^-\pi^+$ is fixed in magnitude and has now two possible orientations consistent with our previous considerations. These are shown in the figure and correspond to $\phi_S=\pm 104$ deg. Inspection of the $\Sigma^-\pi^+$ angular distribution allows a choice between these two alternatives: $\phi_S=-104$ deg requires a $\sin^2\theta$ below resonance changing rapidly to a $\cos^2\theta$ above resonance; $\phi_S=+104$ deg demands the opposite behavior. The experimental data in Fig. 10 clearly require the negative sign.[23] The $\Sigma^0\pi^0$ angular distribution is also predictable. A complete vector diagram of all amplitudes obtained in the computer fit appear later (Fig. 39), as well as these fits to the data (Figs. 26 through 38).

All S and resonant D_3 amplitudes have now been fixed by the cross-section and angular-distribution data. The $\sin\theta\cos\theta$ polarization coefficient given by $B_1=6\,\mathrm{Im}(S^*D_3)$ is then predicted. From Fig. 23, $\alpha_0 B_1$ for for Σ^+ must be positive below resonance, passing through zero and becoming negative above resonance. Referring ahead to Fig. 36, we have plotted the experimentally measured quantity representing the average value of the $\sin\theta\cos\theta$ term times $\alpha_0=-1$. The behavior of this term is just as predicted from the angular distribution for $S-D_3$ interference. If the parity assignment had been $KN\Sigma$ even, then the dominant $\Sigma\pi$ states would have been P_1 and P_3 rather than S and D_3. This would have led to the opposite sign for the interference term. The solid curve in the figure is obtained from the computer fit for the assumption of negative $KN\Sigma$ parity and contains in addition to the dominant $S-D_3$ amplitudes, small amounts of P_1 and P_3 amplitudes required by the least-squares fit. This yields a very satisfactory $\chi^2=14.6$, when about 13 is expected. The dashed curve for positive parity has a χ^2 value of 65, or a probability of less than 10^{-6} of being correct. This leads to the conclusion of negative $KN\Sigma$ parity.

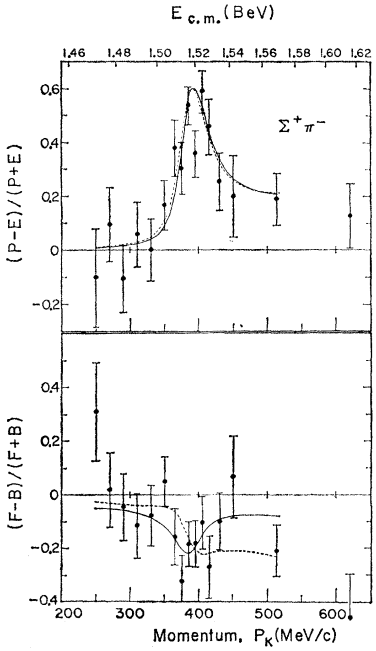

FIG. 32. Polar-equatorial and front-back ratios for $\Sigma^+\pi^-$ as a function of momentum.

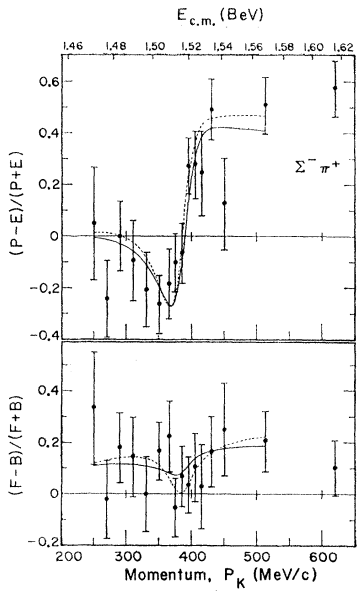

FIG. 33. Polar-equatorial and front-back ratios for $\Sigma^-\pi^+$ as a function of momentum.

A further argument involving P_3-D_3 interference and leading to the same parity conclusion is presented in Sec. VIII. The degree to which these conclusions depend on the assumptions made in the analysis is discussed in Sec. IX.

VII. COMPUTER ANALYSIS

A. Partial-Wave Equations

The differential cross section I and the product $I\mathbf{P}$ of the differential cross section and polarization can be written as $I=|f|^2+|g|^2$ and $I\mathbf{P}=2\,\mathrm{Re}f^*g\hat{n}$, where $\hat{n}=\mathbf{K}_i\times\mathbf{K}_f/|\mathbf{K}_i\times\mathbf{K}_f|$ is the normal to the scattering plane, and f and g, expanded in partial waves, become[24]

$$f(\theta)=\frac{(4\pi)^{1/2}}{K}\sum_{l=0}^{\infty}(2l+1)^{-1/2}[(l+1)T_l^+ + lT_l^-]Y_l^0 \quad (14)$$

and

$$g(\theta)=i\frac{(4\pi)^{1/2}\sin\theta}{K}\frac{\partial}{\partial(\cos\theta)}\times\sum_{l=0}^{\infty}(2l+1)^{-1/2}[T_l^+ - T_l^-]Y_l^0. \quad (15)$$

[23] The low-energy $K-p$ experiment of Humphrey and Ross is sensitive to this sign in a somewhat indirect way involving charge-dependent effects near the $\bar{K}^0n$ threshold. Their solution 1, which fits their and our data somewhat better, has however a positive sign for ϕ_S while their solution 2 has a negative sign in accord with our experiment. This was first pointed out by T. Akiba and R. H. Capps, Phys. Rev. Letters 8, 457 (1962).

[24] J. V. Lepore, Phys. Rev. 79, 137 (1950). His choice of normal is opposite to ours, leading to the opposite sign for $g(\theta)$.

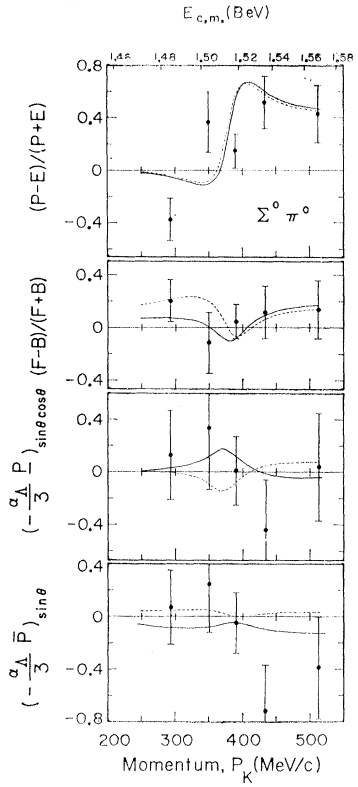

FIG. 34. Polar-equatorial and front-back ratios and the $\sin\theta\cos\theta$ and $\sin\theta$ polarization terms for $\Sigma^0\pi^0$ as a function of momentum.

Here $T_l^{\pm}$ represents the partial-wave amplitude for an orbital angular momentum $J=l\pm\frac{1}{2}$. In the elastic channel this is $T_l=(\eta_l e^{2i\delta_l}-1)/2i$, while for a reaction channel $T_l^{\pm}$ represents the complex amplitude for that l and J. The normalization chosen here (different from our previous letters[3]) is such that the maximum value of T_l is 1 for the elastic channel and 0.5 for a reaction channel. The incident c.m. wave number is $K=1/\lambda=P/\hbar$. We may express I and $I\mathbf{P}$ by a power series in $\cos\theta$:

$$I=\frac{1}{K^2}\sum_{n=0}^{\infty}A_n\cos^n\theta \tag{16}$$

$$I\mathbf{P}=\frac{\hat{n}\sin\theta}{K^2}\sum_{n=0}^{\infty}B_n\cos^n\theta. \tag{17}$$

Expanding Eqs. (14) and (15) through S, P_1, P_3, D_3, and D_5 amplitudes, where $S=T_0$, $P_1=T_1^-$, $P_3=T_1^+$, $D_3=T_2^-$, $D_5=T_2^+$ yields the coefficients:

$$\begin{aligned}
A_0&=|S-D_3|^2+|P_1-P_3|^2\\
&\quad -3\,\mathrm{Re}(S-D_3)^*D_5+9/4|D_5|^2\\
A_1&=2\,\mathrm{Re}(S+2D_3)^*(P_1+2P_3)\\
&\quad -18\,\mathrm{Re}P_3^*D_3-9\,\mathrm{Re}P_1^*D_5\\
A_2&=|S+2D_3|^2-|S-D_3|^2+|P_1+2P_3|^2\\
&\quad -|P_1-P_3|^2+9\,\mathrm{Re}(S-4D_3)^*D_5-\tfrac{9}{2}|D_5|^2\\
A_3&=18\,\mathrm{Re}P_3^*D_3+12\,\mathrm{Re}P_3^*D_5+15\,\mathrm{Re}P_1^*D_5\\
A_4&=45\,\mathrm{Re}D_3^*D_5+45/4|D_5|^2
\end{aligned} \tag{18}$$

$$\begin{aligned}
B_0&=2\,\mathrm{Im}(S-D_3)^*(P_1-P_3)-3\,\mathrm{Im}D_5^*(P_1-P_3)\\
B_1&=6\,\mathrm{Im}S^*D_3-6\,\mathrm{Im}P_1^*P_3-6\,\mathrm{Im}S^*D_5\\
B_2&=18\,\mathrm{Im}P_3^*D_3-15\,\mathrm{Im}P_1^*D_5-3\,\mathrm{Im}P_3^*D_5\\
B_3&=-45\,\mathrm{Im}D_3^*D_5.
\end{aligned} \tag{19}$$

Generally, the analysis is extended only through the D_3 amplitude, except for the case where a D_5 resonance is investigated. This is justified, since the K^-p c.m. momentum at resonance is only 245 MeV/c.

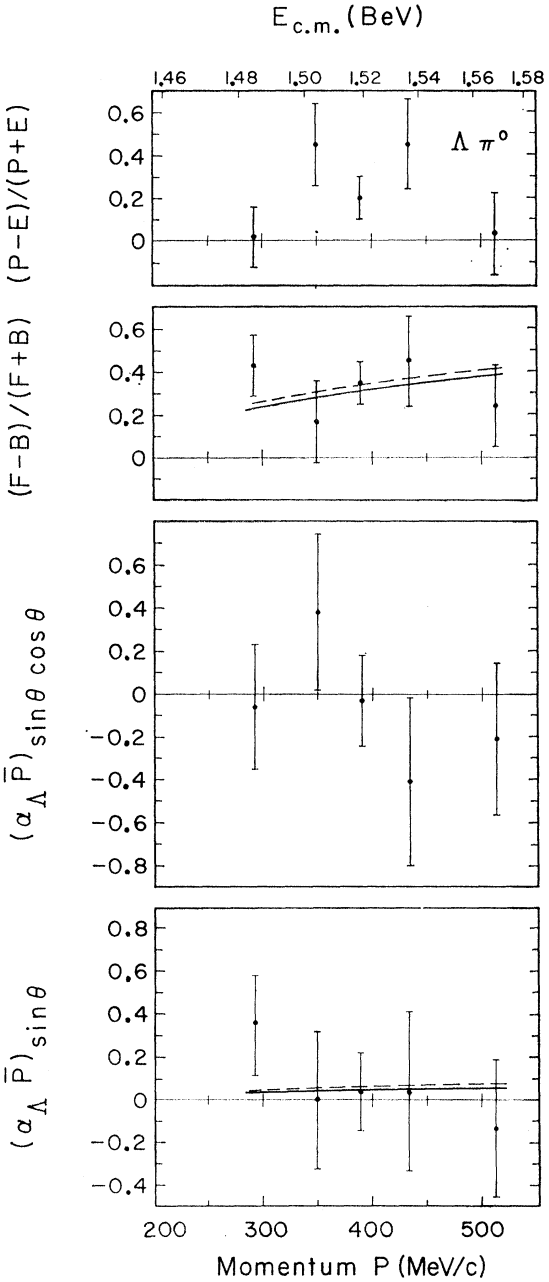

FIG. 35. Polar-equatorial and front-back ratios and the $\sin\theta\cos\theta$ and $\sin\theta$ polarization terms for $\Lambda\pi^0$ as a function of momentum.

B. Resonant Amplitudes

We express the $I=0$, $J=\frac{3}{2}$ resonant amplitudes in the Breit-Wigner form:

$$D_{03}^{\bar{K}N}=\frac{\Gamma_K/\Gamma}{\epsilon-i},$$

$$D_{03}^{\Sigma\pi}=\frac{(\Gamma_K\Gamma_\Sigma/\Gamma^2)^{1/2}}{\epsilon-i}, \tag{20}$$

$$D_{03}^{\Lambda\pi\pi}=\frac{[\Gamma_K(\Gamma-\Gamma_K-\Gamma_\Sigma)/\Gamma^2]^{1/2}}{\epsilon-i},$$

where $\epsilon=(2/\Gamma)(E_R-E)$. The various partial widths have an energy dependence, which nonrelativistically is given by[12]

$$\Gamma\propto\frac{K(KR)^4}{9+3(KR)^2+(KR)^4}, \tag{21}$$

where R corresponds to the channel radius. One power of K in the numerator arises from phase space, while the remaining momentum dependence is due to the D-wave centrifugal barrier. For the first pion-nucleon resonance, $N^*(1238)$, the corresponding formula for a P-wave resonance yields remarkably good agreement with experiment for a radius $R=0.88\lambda_\pi$.[25] Compared to N^*, the $Y_0^*(1520)$ data are sparser, background effects are large, and multichannel complications are present. Thus, we cannot hope to extract the several channel radii from the experimental data. We have instead considered two extreme cases: $\Gamma\propto K^5$ and $\Gamma\propto K$. Both extremes give adequate fits to the data, although the first case is significantly better. Therefore, we have used $\Gamma\propto K^5$ in all subsequent fits for a D_3 resonance. For investigating the possibility of a P_3 resonance in the $\bar{K}N$ system, we have taken $\Gamma\propto K^3$. Since in the vicinity of the resonance the c.m. momenta in the various channels are quite comparable, we have in all cases taken K as the K^-p c.m. wave number.

C. Nonresonant Amplitudes

Dalitz and Tuan[26] have developed the K-matrix formalism to be applied to low-energy K^-p interactions. They show that, to the extent the K-matrix elements are constant and to the approximation that one can neglect the energy dependence of phase-space factors and centrifugal barriers in the exothermic reaction channels, the complex scattering length $A=a+ib$ is a constant in the expression $K^{2l+1}\cot\delta=1/A$. This corresponds to the zero-effective-range approximation. The scattering amplitude in the $\bar{K}N$ channel then becomes

$$T_{I,l}=\frac{K^{2l+1}A_{I,l}}{1-iK^{2l+1}A_{I,l}}. \tag{22}$$

The square of the absorption amplitude for a two-channel process is given by

$$|T_{I,l}|^2=\frac{K^{2l+1}b_{I,l}}{(1+K^{2l+1}b_{I,l})^2+(K^{2l+1}a_{I,l})^2}. \tag{23}$$

In general, however, there are several absorption channels, $\Sigma\pi$, $\Lambda\pi$, and $\Lambda\pi\pi$. To accomodate these we introduce *branching fractions*, r into each channel. In the $\Lambda\pi$ channel, terms through $\cos\theta$ are necessary and perhaps sufficient to describe the angular distribution. For simplicity we limit this channel to S and P_1 amplitudes, both with $I=1$.

In the $\Sigma\pi$ channels nonresonant amplitudes are introduced into all partial waves through D_3 with the exception of the $I=0$, D_3 state. This is excluded because the superposition of a nonresonant amplitude in the same spin, parity, and isotopic spin as a resonant amplitude presents certain additional problems. They are not merely additive, since this would violate unitarity. Consider first a one-channel process. The S matrix element may be written[27] $S=e^{2i\delta}(\epsilon+i)/(\epsilon-i)$, where now δ is a real nonresonant phase shift and clearly $|S|^2=1$. With $S=1+2iT$, the scattering amplitude becomes $T=e^{i\delta}\sin\delta+e^{2i\delta}/(\epsilon-i)$, consisting of a nonresonant term plus a resonant term that is shifted in phase by 2δ. If now we extend this to a multichannel resonance, but with the nonresonant term still elastic (real scattering length),

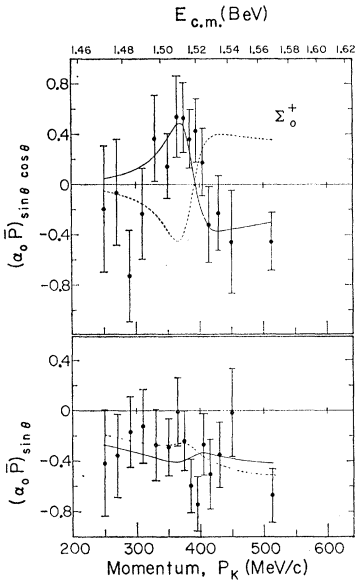

FIG. 36. The $\sin\theta\cos\theta$ and ($\sin\theta$, $\sin\theta\cos^2\theta$) polarization terms for $\Sigma^+\pi^-$, $\Sigma_0^+\to p\pi^0$ as a function of momentum. The solid curves correspond to negative $KN\Sigma$ parity (solution I) and yield a satisfactory fit. The dashed curves correspond to positive $KN\Sigma$ parity (solution V) and for the $\sin\theta\cos\theta$ term is approximately a reflection of solution I, resulting in $\chi^2=65$ when about 13 is expected (probability $<10^{-6}$).

[25] M. Gell-Mann and K. Watson, Ann. Rev. Nucl. Sci. 4, 219 (1954).
[26] R. H. Dalitz and S. F. Tuan, Ann. Phys. (N. Y.) 3, 307 (1960).
[27] L. D. Landau and E. M. Lifshitz, *Quantum Mechanics, Nonrelativistic Theory* (Pergamon Press, Inc., New York, 1958).

the elastic and reaction elements of the T matrix become

$$T_{\alpha\alpha}=e^{i\delta}\sin\delta+\frac{x_\alpha e^{2i\delta}}{\epsilon-i}$$

and (24)

$$T_{\alpha\beta}=\frac{(x_\alpha x_\beta)^{1/2}}{\epsilon-1},$$

where $x_\alpha=\Gamma_\alpha/\Gamma$. We have employed this procedure for introducing a nonresonant D-wave amplitude into the $I=0$ state where the resonance appears. Extending this to a more general case with a three-channel ($\bar{K}N$, $\Sigma\pi$, $\Lambda\pi\pi$) *complex* nonresonant scattering length superposed on a three-channel resonance complicates the formulation if one wishes to preserve unitarity.[28] Since the nonresonant D waves have been found to be small, we feel justified in simplifying the situation. We, thus, take the $I=0$, D_3 scattering length to be real. For the $I=1$ state this problem does not arise, so the scattering length is allowed to be complex.

The expressions for the squares of the *nonresonant* amplitudes in the $\Sigma\pi$, $\Lambda\pi$, and $\Lambda\pi\pi$ channels are then:

$$|S_0^{\Sigma\pi}|^2=\frac{Kb_0}{(1+Kb_0)^2+(Ka_0)^2};$$

$$|S_1^{\Sigma\pi}|^2=\frac{Kb_1(1-r_S^{\Lambda\pi})}{(1+Kb_1)^2+(Ka_1)^2};$$

$$|P_{0,2J}^{\Sigma\pi}|^2=\frac{K^3b_{0,2J}}{(1+K^3b_{0,2J})^2+(K^3a_{0,2J})^2};$$

$$|P_{1,2J}^{\Sigma\pi}|^2=\frac{K^3b_{1,2J}(1-r_{P1,2J}^{\Lambda\pi})}{(1+K^3b_{1,2J})^2+(K^3a_{1,2J})^2};$$

$$|D_{0,3}^{\Sigma\pi}|^2=0;\quad |D_{1,3}^{\Sigma\pi}|^2=\frac{K^5b_{1,3}r_{D13}^{\Sigma\pi}}{(1+K^5b_{1,3})^2+(K^5a_{1,3})^2};$$

$$|S_1^{\Lambda\pi}|^2=\frac{Kb_1r_S^{\Lambda\pi}}{(1+Kb_1)^2+(Ka_1)^2}; \tag{25}$$

$$|P_{1,1}^{\Lambda\pi}|^2=\frac{K^3b_{1,1}r_{P1,1}^{\Lambda\pi}}{(1+K^3b_{1,1})^2+(K^3a_{1,1})^2};$$

$$|P_{1,3}^{\Lambda\pi}|^2=0;\quad |D_{1,3}^{\Lambda\pi}|^2=0;$$

$$|S_I^{\Lambda\pi\pi}|^2=0;\quad |P_{I,2J}^{\Lambda\pi\pi}|^2=0;$$

$$|D_{0,3}^{\Lambda\pi\pi}|^2=0;\quad \text{for}\quad I=0,1;$$

$$|D_{1,3}^{\Lambda\pi\pi}|^2=\frac{K^5b_{1,3}(1-r_{D1,3}^{\Sigma\pi})}{(1+K^5b_{1,3})^2+(K^5a_{1,3})^2}.$$

[28] The general problem can be treated using the K-matrix formalism, the simpler two-channel case being only slightly more involved than the restricted problem which we treat [R. H. Dalitz (private communication)].

The phase angles associated with these various nonresonant amplitudes are not calculable theoretically in any elementary way. They have been introduced as free parameters to be determined by the experimental data. In the spirit of the constant-scattering-length approximation they are assumed to be constant over the 250- through 513-MeV/c momentum region. Figure 24 shows how these phase angles are defined relative to the resonant D amplitude.

D. Isotopic-Spin Composition

Having calculated the isotopic spin amplitudes in the various channels, we may combine these with the proper Clebsch-Gordan coefficients to form the complete amplitude for each charge state. For a partial-wave amplitude T, these are written:

$$T_{K^-p}=\tfrac{1}{2}(T_0^{\bar{K}N}+T_1^{\bar{K}N})$$

$$T_{\bar{K}^0N}=\tfrac{1}{2}(T_0^{\bar{K}N}-T_1^{\bar{K}N})$$

$$T_{\Sigma^+\pi^-}=\frac{1}{\sqrt{2}}\left(\frac{1}{\sqrt{3}}T_0^{\Sigma\pi}-\frac{1}{\sqrt{2}}T_1^{\Sigma\pi}\right)$$

$$T_{\Sigma^-\pi^+}=\frac{1}{\sqrt{2}}\left(\frac{1}{\sqrt{3}}T_0^{\Sigma\pi}+\frac{1}{\sqrt{2}}T_1^{\Sigma\pi}\right)$$

$$T_{\Sigma^0\pi^0}=\frac{1}{\sqrt{2}}\left(-\frac{1}{\sqrt{3}}T_0^{\Sigma\pi}\right) \tag{26}$$

$$T_{\Lambda\pi^\pm\pi^\mp}=\frac{1}{\sqrt{2}}\left(\frac{1}{\sqrt{3}}T_0^{\Lambda\pi\pi}\mp\frac{1}{\sqrt{2}}T_1^{\Lambda\pi\pi}\right)$$

$$T_{\Lambda\pi^0}=\frac{1}{\sqrt{2}}(T_1^{\Lambda\pi}).$$

E. Representation of the Data

In this section we discuss the manner in which the experimental data were introduced into the computer program.

The cross-section data for each channel were generally divided into 20-MeV/c intervals. The $\Lambda\pi^0$ and $\Sigma^0\pi^0$ channels could not be so divided for reasons discussed in Sec. III. In the $\bar{K}^0n$ and $\Lambda\pi^+\pi^-$ channels, the incident momentum was more precisely determined so that, in the resonance region where sufficient data were obtained, finer intervals could be used. Since path lengths were established by the number of τ decays per momentum interval, in channels with large cross sections the statistics on τ decays were the dominant uncertainty (the τ "cross section" at 390 MeV/c is 5.6 mb for a hydrogen bubble chamber).

Because of the narrowness of the resonance, the angular distributions were divided into 10-MeV/c intervals so as not to lose information on the rapid momentum dependence of the resonant amplitudes. For

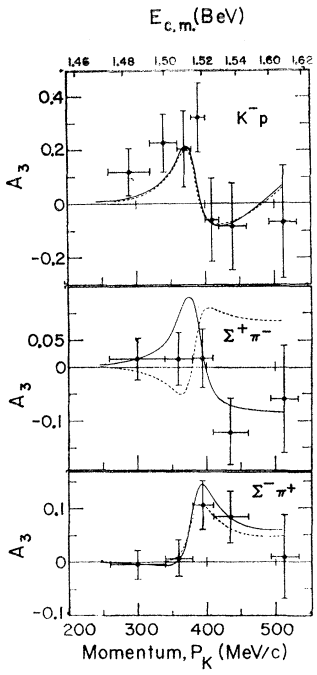

FIG. 37. Coefficients of $\cos^3\theta$ arising from P_3-D_3 interference. They are obtained from a least-squares fit for the angular distributions for K^-p, $\Sigma^+\pi^-$, and $\Sigma^-\pi^+$ taken over wider momentum intervals than the preceding figures. The dashed curve (positive $KN\Sigma$ parity) for $\Sigma^+\pi^-$ fits poorly with $\chi^2=17.5$, when about 4.4 is expected (probability $\approx 2\times 10^{-3}$). This is the second experimental result favoring negative $KN\Sigma$ parity.

example, Fig. 33 shows that the $\Sigma^-\pi^+$ angular distribution changes strikingly from mainly $\sin^2\theta$ to $\cos^2\theta$ within 40 MeV/c. Typical measurement uncertainties on the momentum of each event are about ± 10 MeV/c, so we are justified in subdividing to this extent.

However, divided in such fine momentum intervals, the data in many channels becomes rather sparse, and it is difficult to analyze in a power series expansion through $\cos^3\theta$. In our initial efforts, therefore, we analyzed only through $\cos^2\theta$ with some success, but the P_3-D_3 interference is sufficiently large as to yield significant distortions of the $\cos\theta$ term in certain cases. To overcome this difficulty one could either take larger momentum intervals and lose momentum information, or analyze the angular distribution in terms of polar-equatorial and front-back ratios, the front-back ratio being a combination of A_1 and A_3. The latter course was chosen, although it resulted in the appearance of a number of ambiguities involving even-odd angular momentum interference terms. The expressions for these ratios in terms of the angular-distribution expansion coefficient through A_4 are

$$\frac{F-B}{F+B}=-\frac{1}{2}\frac{A_1+\frac{1}{2}A_3}{A_0+\frac{1}{3}A_2+\frac{1}{5}A_4} \tag{27}$$

and

$$\frac{P-E}{P+E}=-\frac{1}{4}\frac{A_2+\frac{3}{4}A_4}{A_0+\frac{1}{3}A_2+\frac{1}{5}A_4}. \tag{28}$$

Notice that in Eqs. (18) the P_3-D_3 interference is opposite in sign for A_1 and A_3, and that it nearly cancels when the data are expressed in terms of front-back ratios. Thus, we have, in effect, suppressed most of this interference in the fitting procedure. To restore this information we introduced into the program the coefficient A_3 for K^-p, $\Sigma^+\pi^-$, and $\Sigma^-\pi^+$, and B_2 for $\Sigma^+\pi^-$ obtained from data averaged over considerably wider momentum intervals. This sufficed to resolve many of the ambiguities among the small P_1 and P_3 amplitudes. There is a redundancy in utilizing this P_3-D_3 interference data twice, but it is felt that a more realistic evaluation of the various amplitudes entering into the problem is thereby obtained. Fits were also made without this additional data, with very similar results.

The polarization data were handled in the following manner. Limiting the maximum complexity in θ to that obtainable from $J=\frac{3}{2}$, one has

$$I(\theta)P(\theta)=x^2\sin\theta[B_0+B_1\cos\theta+B_2\cos^2\theta].$$

Figure 25 shows these three angular dependences. Integrating over all production angles, one obtains a measure of B_0 and B_2 only since the average value of $\sin\theta\cos\theta$ vanishes. If we average over all θ, we have $\langle\sin\theta\rangle_{\rm av}=\pi/4$ and $\langle\sin\theta\cos^2\theta\rangle_{\rm av}=\pi/16$. The computer calculates the average value of the polarization from

$$\langle P(\theta)\rangle_{\rm av}=\frac{\langle I(\theta)P(\theta)\rangle_{\rm av}}{\langle I(\theta)\rangle_{\rm av}}=\frac{\pi}{4}\left(B_0+\frac{B_2}{4}\right)\Big/\left(A_0+\frac{A_2}{3}\right). \tag{29}$$

This is then compared with the experimental data obtained from Eq. (3) summed over all production angles θ. A measure of B_1 was obtained by summing Eq. (3) over the angular interval $0.95\geqslant\cos\theta\geqslant 0.30$ and subtracting from it the sum over the interval $-0.95\leqslant\cos\theta\leqslant -0.30$. The interval from 0.95 to 0.30 was chosen to eliminate regions where the $\sin\theta\cos\theta$ polarization is small. Over this interval we have $\langle\sin\theta\cos\theta\rangle_{\rm av}=0.429$. The computer then calculated the average value of this polarization term from

$$\langle P(\theta)\rangle_{\rm av}=0.429B_1/(A_0+0.426A_2). \tag{30}$$

In order to investigate the $J=\frac{5}{2}$ resonance possibility, the experimental data were handled in the same way with the computer calculations extended in the obvious manner.

F. The χ^2 Minimization

The computer program calculated each measured quantity for a given set of parameters. The calculated quantities C_i and observed quantities O_i were compared and the χ^2 obtained from $\chi^2=\sum_i(C_i-O_i)^2/\delta O_i^2$, where δO_i is the statistical uncertainty. The χ^2 function was minimized by the "method of ravines," using a program written by W. E. Humphrey. Briefly, this procedure involves the following steps. From a point A compute the gradient. Move along the gradient direction a predetermined distance to point B. At B compute the gradient and determine the projection of this gradient on the hyperplane perpendicular to the line AB. Move in the direction of this projection a predetermined dis-

TABLE IX. Parameters at the minima obtained by the computer for various assumptions.

Parameter[b]	Meaning	Solutions[a] I	II	III	IV	V	VI	VII	VIII	IX	Diagonal error
a_0	s scattering length	0.081	0.043	−1.700	0.561	−0.450	−1.749	−1.717	−0.226	−0.162	0.5
b_0	s scattering length	3.133	3.351	1.722	3.210	3.000	1.429	0.669	0.278	3.443	0.8
a_1	s scattering length	0.017	0.037	−0.124	0.016	0.030	−0.130	−0.217	−1.320	0.039	0.08
b_1	s scattering length	0.459	0.473	0.432	0.460	0.469	0.428	0.377	0.899	0.456	0.03
$r_{S1}^{\Lambda\pi}$	$\left(\frac{\sigma(\Lambda\pi)}{\sigma(\Lambda\pi)+\sigma(\Sigma\pi)}\right)_{S_1}$	0.287	0.289	0.303	0.290	0.268	0.296	0.318	0.426	0.291	0.03
ϕ_{S0-S1}	S_0-S_1 $\Sigma-\pi$ angle	−1.808	−1.784	−1.856	−1.846	−1.814	−1.627	+1.545	−1.939	−1.857	0.12
a_{01}	p_1 scattering length	0.0350	0.0471	0.1431	0.0180	0.0478	0.1655	0.1597	0.0866	0.0333	0.06
b_{01}	p_1 scattering length	0.0042	0.0056	0.0045	0.0038	0.0065	0.0132	0.0494	0.0624	0.0214	0.004
a_{11}	p_1 scattering length	−0.0420	−0.0373	0.0412	−0.0283	−0.0376	0.0476	0.0360	0.2186	0.0050	0.023
b_{11}	p_1 scattering length	0.0092	0.0106	0.0117	0.0090	0.0083	0.0121	0.0261	0.0654	0.0139	0.004
$r_{P11}^{\Lambda\pi}$	$\left(\frac{\sigma(\Lambda\pi)}{\sigma(\Lambda\pi)+\sigma(\Sigma\pi)}\right)_{P_{11}}$	0.501	0.425	0.392	0.489	0.673	0.413	0.201	0.103	0.332	0.22
ϕ_{P01}	P_{01} phase angle	3.897	4.104	4.243	4.105	4.616	4.583	3.961	2.161	1.196	0.28
ϕ_{P11}	P_{11} phase angle	1.521	1.496	1.810	1.701	2.468	1.810	1.167	3.720	3.151	0.41
E_R	Resonant energy	1519.41	1518.85	1519.34	1518.50	1518.46	1517.53	1516.45	1519.17	1518.45	0.87
Γ	Full width	16.426	16.829	15.522	17.297	16.955	17.936	10.358	20.338	18.385	1.20
Γ_K	$\bar{K}-N$ partial width	4.806	4.840	4.596	4.910	4.430	5.139	3.292	1.411	2.850	0.43
Γ_Σ	$\Sigma-\pi$ partial width	8.967	9.349	8.988	9.755	9.304	10.059	5.332	9.691	12.001	1.05
ϕ_{S1-D}	S_1-D relative phase	−2.158	−2.090	−1.911	−2.024	−2.152	−2.175	+3.254	−0.739	−2.064	0.12
$\phi_{SP1}^{\Lambda\pi}$	$S-P_1$ phase $\Lambda\pi$ channel	0.154	0.150	0.151	0.150	0.179	0.161	0.163	0.137	0.152	0.31
a_{03}	p_3 scattering length	0.0996	0.0833	0.0565	0.0926	0.1021	0.0408	0.0658	0.0273	0.0985	0.10
b_{03}	p_3 scattering length	0.0062	0.0079	0.0132	0.0073	0.0068	0.0067	0.0115	0	0.0004	0.003
a_{13}	p_3 scattering length	0.0409	0.0296	0.0030	0.0309	0.0424	−0.0002	0.0135	0.1133	0.0266	0.007
b_{13}	p_3 scattering length	0.0041	0.0039	0.0063	0.0048	0.0011	0.0079	0.0113	0.0106	0.0036	0.003
ϕ_{P03}	P_{03} phase angle	1.026	1.271	1.504	1.190	2.417	2.611	3.602	0	3.585	0.26
ϕ_{P13}	P_{13} phase angle	2.859	3.093	2.991	2.963	0.361	−0.857	1.487	4.441	1.961	0.66
a_{D03}	d_3 scattering length	0.0168	0.0142	0.0154	0	0.0139	0.0224	0.0124	0.0016	−0.0008	0.01
b_{D03}	d_3 scattering length	0	0	0	0	0	0	0	0.0001	0.0003	0
a_{D13}	d_3 scattering length	0.0016	−0.0041	0.0078	0	−0.0007	0.0060	0.0038	−0.0044	−0.0015	0.01
b_{D13}	d_3 scattering length	0.0021	0.0023	0.0031	0.0020	0.0022	0.0028	0.0026	0.0034	0.0018	0.001
ϕ_{D03}	D_{03} phase angle	0	0	0	0	0	0	0	−0.972	−1.106	0
ϕ_{D13}	D_{13} phase angle	−1.092	−1.472	−1.046	0	−2.552	−1.973	−1.935	−0.046	−2.886	1.12
$r_{D13}^{\Sigma\pi}$	$\left(\frac{\sigma(\Sigma\pi)}{\sigma(\Sigma\pi)+\sigma(\Lambda\pi\pi)}\right)_{D_{13}}$	0.089	0.138	0.258	0	0.239	0.343	0.035	0.100	0.0001	0.18

[a] Solution I: Negative $KN\Sigma$ parity. Minimized including A_3, B_2 coefficients. Solution II: Negative $KN\Sigma$ parity. Minimized without A_3, B_2 coefficients. Solution III: Negative $KN\Sigma$ parity. Width $\Gamma \propto K$. Solution IV: Negative $KN\Sigma$ parity. Without nonresonant D_3 amplitudes. Solution V: Positive $KN\Sigma$ parity. Minimized including A_3, B_2 coefficients. Solution VI: Positive $KN\Sigma$ parity. Minimized without A_3, B_2 coefficients. Solution VII: Positive $KN\Sigma$ parity. Quasiminimum. Solution VIII: Positive $KN\Sigma$ parity. Resonance in P_3, K^-p state. Solution IX: Positive $KN\Sigma$ parity. Resonance in D_5, K^-p state.
[b] Scattering lengths are expressed in $(F)^{2l+1}$ energies and widths in MeV, and phase angles in rad.

tance to point C. Using the value at point B, the derivatives at B, and the value at point C, calculate the distance to a minimum, assuming a parabolic dependence of χ^2 as a function of distance along this new direction. Move to this minimum and begin the process again. Each complete step takes approximately 30 sec when the IBM 7090 is used.

The method tends to move along ravines toward minima rather than oscillating between the ravine walls. Even so, typically several hours of computation are required in order to arrive at a minimum in this 30-dimensional χ^2 space starting from reasonable initial values.

VIII. COMPUTER RESULTS

A. Negative $KN\Sigma$ Parity

The search for solutions compatible with the experimental data proceeded in the following way. The nonresonant S and resonant D_3 amplitudes obtained by the precomputer analysis were introduced as starting conditions along with zero initial nonresonant P_1, P_3, and D_3 amplitudes. With all parameters varying, a satisfactory solution was found with $\chi^2=221.5$. This fit contained 257 data points, including the coefficients A_3 and B_2. With 30 parameters the expected χ^2 is $257-30=227$, which is in good agreement with the value obtained. Because of the slight redundancy associated with the introduction of A_3 and B_2 coefficients, we also minimized χ^2, eliminating these data points. With 235 data points we obtained a χ^2 of 208 when 205 was expected. The probability of a fit with χ^2 this large or larger is 43%. The parameters for these two fits appear as solutions I and II of Table IX. The contributions to χ^2 for the various measured quantities in each channel are shown in Table X. Apart from the $\Sigma^0\pi^0$ polar-equatorial ratios, each line yields a satisfactory χ^2, so that to within the precision of the experiment the parametrization by constant scattering lengths over this momentum region is adequate. In Figs. 26 through 38, we display the momentum dependence of all data; the solid lines are obtained from solution I. The fits extend over the

TABLE X. Chi-square contributions for each solution according to various channels and measurements. The solutions are explained in the footnote of Table IX.

Measured quantity	Reaction	Data points	Solutions[a] I	II	III	IV	V	VI	VII	VIII	IX
σ	K^-p	12	12.53	12.27	12.08	12.61	12.67	12.56	12.57	23.40	13.11
	$\bar{K}^0n$	10	12.82	13.18	12.43	15.13	15.17	11.31	13.18	33.80	**21.12**
	$\Sigma^+\pi^-$	12	7.38	6.12	7.52	7.26	8.58	4.39	6.24	7.99	7.22
	$\Sigma^-\pi^+$	12	12.80	11.51	10.88	13.89	12.29	10.19	8.29	16.30	13.43
	$\Sigma^0\pi^0$	5	9.27	11.00	7.54	10.01	9.42	12.00	16.46	33.47	11.42
	$\Lambda\pi^0$	5	4.20	4.06	4.28	4.14	4.81	4.38	4.39	1.71	4.18
	$\Lambda\pi\pi$	11	8.76	9.00	17.00	9.18	11.26	11.80	14.77	10.55	10.26
$(F-B)/(F+B)$	K^-p	15	13.00	12.73	11.38	13.18	12.35	10.89	11.68	17.32	13.90
	$\bar{K}^0n$	9	2.80	2.68	2.53	3.57	2.74	2.92	4.41	10.08	2.92
	$\Sigma^+\pi^-$	15	15.09	13.77	14.87	14.42	18.48	15.82	16.94	32.36	14.24
	$\Sigma^-\pi^+$	15	6.88	6.93	7.56	6.64	5.93	7.33	7.57	11.64	7.96
	$\Sigma^0\pi^0$	5	2.30	2.36	2.64	2.26	2.79	3.75	7.51	7.08	1.83
	$\Lambda\pi^0$	5	3.35	3.45	3.41	3.47	3.03	3.19	3.11	3.03	3.40
$(P-E)/(P+E)$	K^-p	15	16.59	16.39	18.31	16.37	18.90	17.05	24.03	75.61	23.27
	$\bar{K}^0n$	9	2.08	2.16	3.14	2.34	1.86	2.48	2.84	**31.41**	1.51
	$\Sigma^+\pi^-$	15	17.22	16.31	16.18	17.08	16.75	14.53	**113.53**	30.31	21.03
	$\Sigma^-\pi^+$	15	12.03	12.56	13.34	11.18	12.35	12.11	19.16	32.05	13.06
	$\Sigma^0\pi^0$	5	16.67	15.99	13.08	17.06	18.01	17.28	16.28	14.89	17.54
$\langle\alpha P\rangle_{\sin\theta,\sin\theta\cos^2\theta}$	$\Sigma^+\pi^-$	15	11.66	12.08	11.09	10.67	10.23	9.55	7.64	21.89	11.75
	$\Sigma^0\pi^0$	5	4.54	45.54	4.09	4.50	5.78	5.62	4.26	4.86	4.63
	$\Lambda\pi^0$	5	2.19	2.20	2.19	2.20	2.16	2.18	2.17	2.18	2.19
$\langle\alpha P\rangle_{\sin\theta\cos\theta}$	$\Sigma^+\pi^-$	15	14.57	14.83	18.80	15.00	**65.17**	**60.14**	14.54	22.34	15.01
	$\Sigma^0\pi^0$	5	1.73	1.79	1.66	1.78	2.81	2.67	1.42	1.86	1.71
Sum		235	211.82	207.89	216.00	213.97	273.54	254.11	332.98	446.09	236.69
A_3	K^-p	7	6.18				7.44		11.33		
	$\Sigma^+\pi^-$	5	2.57				**17.50**		**16.93**		
	$\Sigma^-\pi^+$	5	0.96				0.49		2.71		
B_2	$\Sigma^+\pi^-$	5	1.37				1.17		2.29		
Sum		257	221.52	226.87		231.77	300.11	349.23	366.24		

[a] Bold-faced numerals indicate values where solutions V, VI, VII, and IX are in serious disagreement with the data.

interval 250 to 513 MeV/c. The points at 620 MeV/c were kindly supplied by P. Bastien before publication and are shown only to indicate the continued trend of the data.

Figure 39 shows the vectors representing the magnitudes and phases of the various amplitudes of solution I at the resonant energy as they appear in the $\bar{K}N$ and $\Sigma\pi$ channels. The S and resonant D_3 amplitudes are clearly dominant. The real and imaginary parts of the K^-p forward scattering amplitude as obtained from solution I appear in Figure 40.

Two extreme assumptions were made for the energy dependence of the resonance widths $\Gamma \propto K^5$ and $\Gamma \propto K$ corresponding to a small ($R<\lambda\pi/2$) and to a very large ($R>2\lambda\pi$) radius of interaction. The solutions discussed above used $\Gamma \propto K^5$. The widths appearing in Table IX are the widths at resonance, i.e., they correspond to Γ_0 in $\Gamma=\Gamma_0(K/K_0)^5$, where K_0 is the wave number at resonance. The fit using $\Gamma \propto K$ appears as solution III in Tables IX and X. It is somewhat poorer than for $\Gamma \propto K^5$, having a χ^2 of 216 rather than 208, the major difference occurring in the $\Lambda\pi\pi$ channel. Accordingly, we have employed $\Gamma \propto K^{2l+1}$ for all other solutions.

Apart from the S wave, no single nonresonant amplitude was sufficiently large to be significant in itself. We also minimized χ^2 by setting all nonresonant D_3 waves to zero (except for the nonresonant $\Lambda\pi\pi$). With four fewer parameters, χ^2 increased by six, indicating that although nonresonant D waves do improve the fit, they are not necessary. This is solution IV in Tables IX and X.

When the coefficients A_3 are not retained, a number of ambiguities arise among the small P-wave amplitudes. For example, interchanging P_1 and P_3 amplitudes in the $\bar{K}N$ channels and reminimizing yields a result almost as good as that of solution II. However, since P_3 was initially considerably larger than P_1, the coefficient $A_3=18\,\mathrm{Re}(P_3{}^*D_3)$ in the K^-p channel then becomes much smaller than the observed value. Similar ambiguities exist in the $\Sigma\pi$ channels. By making various interchanges of the $\Sigma\pi$ phase angles in the P states followed by a reminimization, one can obtain solutions with somewhat higher although acceptable χ^2. However, these new solutions yield a momentum dependence for the A_3 coefficients opposite to that observed for $\Sigma^+\pi^-$, $\Sigma^-\pi^+$, or both. Accordingly, by use of the A_3 and B_2 coefficients, we have found what appears to be a definitely best solution. On the other hand, some of the ambiguities associated with these small P waves do not differ sufficiently from the data so as to be completely excluded statistically. For brevity, we do not include these ambiguities in the tables, but list only the best solution under various assumptions.

B. Positive $KN\Sigma$ Parity

The equations used in the computer fit were written for negative $KN\Sigma$ parity. Since a change of parity changes only the sign of the polarization terms, the positive-parity assumption was explored by changing the sign of the helicity, α, for Σ decays. Starting from solution I with the polarization terms reversed, χ^2 was again minimized. Because of the variety of ambiguities associated with the P amplitudes, an equally satisfactory fit was quickly obtained for the $\sin\theta$, $\sin\theta\cos^2\theta$ term in polarization by a reorientation of these amplitudes. However, as discussed previously, no such reorientation is possible for the Σ^+ S amplitude, the relative $S-D_3$ angle being fixed by the strong appearance of $\cos^2\theta$ in the Σ^+ angular distribution at resonance. As a result, the lowest χ^2 fit yields a $\sin\theta\cos\theta$ term in Σ_0^+ polarization not differing markedly from a mere reflection of the negative $KN\Sigma$ parity curve as seen in Fig. 36.

Solutions V and VI of the Tables IX and X list the best fits for positive $KN\Sigma$ parity including and excluding the A_3, B_2 data, respectively. With the exception of the $\sin\theta\cos\theta$ term in Σ^+ (and Σ^0) polarization and the A_3 coefficient in the Σ^+ angular distribution, all data can be equally well fitted to positive $KN\Sigma$ parity; this can be seen from Table X or from Figs. 26 through 38, where the dashed lines are obtained from solution V. All additional χ^2 comes from the polarization data and from A_3. Within the framework of the analysis, the positive $KN\Sigma$ parity assumption clearly disagrees with the data.

The $\sin\theta\cos\theta$ polarization term has been discussed already. Let us look at the A_3 and B_2 coefficients given by $A_3=18\,\mathrm{Re}(P_3{}^*D_3)$ and $B_2=18\,\mathrm{Im}(P_3{}^*D_3)$. Because of their simplicity, they are free of the ambiguities associated with analysis in terms of F–B and P–E ratios. The behavior of the A_3 data demands that the P_3 amplitude vector appear to the right of the D_3 amplitude at resonance, whereas for positive $KN\Sigma$ parity, the B_2 polarization term demands the opposite behavior.

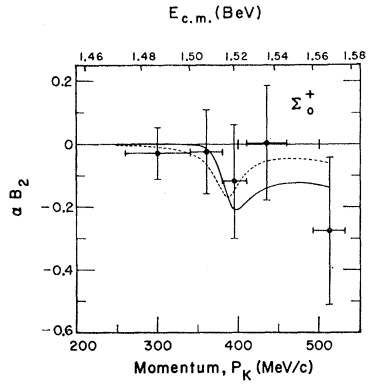

FIG. 38. Least-squares fit to the Σ_0^+ polarization yields for the $\sin\theta\cos^2\theta$ term, the coefficient B_2 coming from P_3-D_3 interference. We plot $\alpha_0 B_2$, where α_0 equals -1 as a function of momentum. Both parity cases fit well, but because of the correlation with the Σ^+ angular distribution (Fig. 37), the A_3 term is of necessity fit poorly.

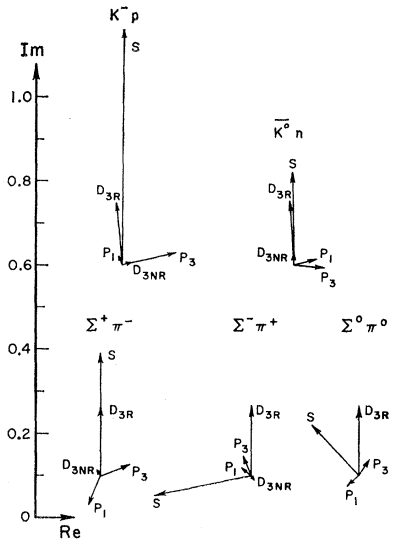

FIG. 39. Magnitudes and phases for the S, P_1, P_3, and D_3 amplitudes for the $\bar{K}^-p$, $\bar{K}^0n$, $\Sigma^+\pi^-$, $\Sigma^-\pi^+$, and $\Sigma^0\pi^0$ channels at resonance as given by solution I. The scale for the amplitudes (dimensionless) appears to the left. The maximum possible value of the amplitudes is one for the $\bar{K}^-p$ channel.

Minimization of the over all χ^2 has resulted in a good fit to the B_2 polarization term and a poor fit to A_3. Since one is dealing here with a small P_3 interference term, the argument is not as strong as that involving $S-D_3$ interference. None the less, it is very encouraging to find that the P_3-D_3 interference fits negative $KN\Sigma$ parity nicely and confirms the argument based on the $S-D_3$ interference.

Attempts were made to find other unrelated solutions which would be compatible with the observed behavior. An exhaustive search of a 30-dimensional space was deemed out of the question. However, the dominant $S-D_3$ terms are the only ones that can seriously affect the $P-E$ and $\sin\theta\cos\theta$ polarization data. We have reoriented the amplitudes in various possible ways, always returning to minima in the vicinity of that discussed above. For example, by reversing the $S-D_3$ phase angle for Σ^+ one can obtain a rather good fit to the $\sin\theta\cos\theta$ polarization term, to the detriment of the well-measured Σ^+ angular distribution. This can be seen from Fig. 23. If one performs this reversal by a reflection of the S-wave triangle in the figure through the horizontal axis, then to a first approximation the trend of the Σ^- angular distribution remains the same. In terms of the computer parameters this corresponds to a reversal of sign of ϕ_{S0-S1}, and ϕ_{S1-D}. But reversal of the Σ^+ S amplitude yields a negative P–E ratio at resonance rather than the strong positive term observed. This can be partially compensated by enlarged nonresonant D waves and more nonresonant P_1-P_3 interference. However, since the angular distributions are well measured, the χ^2 always remains poor. The computer has found a quasi-minimum with the above properties but with a large

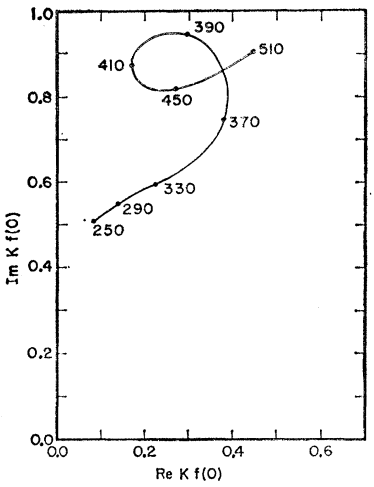

FIG. 40. Real and imaginary parts of $kf(0)$, where $f(0)$ is the forward scattering amplitude. The curve is obtained from solution I, the numbers are K^-p laboratory momenta.

$\chi^2=366$. This is listed in the tables as solution VII. This solution yields an approximately stationary χ^2, the good polarization fit being balanced by the poor angular distribution, but eventually the computer returned this solution to the lower χ^2 of solution V.

C. The P_3 Resonance Possibility

In order to investigate quantitatively the strength of our arguments concerning the identification of the incident K^-p resonant state as a D wave, we modified the computer program to introduce the resonant amplitude in the P_3 state. The resonance widths were correspondingly taken to be proportional to K^3 for a P-wave resonance. Very poor fits to the data were obtained for both parity assumptions. The better of the two (positive $KN\Sigma$ parity) is solution VIII. A χ^2 value of 446 was obtained where 205 was expected.

D. The $J=\frac{5}{2}$-Resonance Possibility

Referring to Eqs. (14) and (15), notice that under the interchange $T_l^+ \rightleftarrows T_l^-$, $g(\theta)$ changes in sign only, while $f(\theta)$ remains approximately the same. Let us focus our attention on the dominant S state (which does not appear in g) and the resonant D state. Perform this interchange on the resonant amplitude only, i.e., $D_3 \rightarrow D_5$; the angular distribution remains the same, to a first approximation, and the sign of IP changes. Thus, one is led to suspect that if the resonance were to have a spin of $\frac{5}{2}$ rather than $\frac{3}{2}$, the parity arguments would be reversed. To quantitatively investigate this important possibility we have modified the computer program to include the D_5 amplitude as a resonant term. All nonresonant amplitudes through D_3 were included. Additional terms containing the coefficients A_4 and B_3 were introduced into the $P-E$, $F-B$, and polarization terms, and a fit was made to positive $KN\Sigma$ parity. The $\Sigma\pi$ resonant state is thus assumed to be F_5. The results are shown as solution IX in Tables IX and X. A χ^2 value of 237 is obtained with 203 expected, which has a confidence level of 5%. All data fit well (including the unfitted A_3, B_2 terms), with the sole exception of the $\bar{K}^0n$ cross-section channel shown in Fig. 41. Because the D_5 resonance is considerably more effective in producing strong $P-E$ effects, the fit has greatly reduced the magnitude of the resonance ($x=0.15$ compared to $x=0.29$ for a D_3 resonance). The result is a 1-mb enhancement in the $\bar{K}^0n$ channel, where experiment suggests about 5 mb. The probability of this curve fitting the data is about 1%.

A further consideration is the magnitude of the A_4 coefficient generated by the D_5 resonance. This does not appear explicitly in the program but is mixed with A_0 and A_2 terms in the P–E ratio. However, no significant A_4 terms are found in the experimental data. To improve statistics we have taken wider momentum intervals in the Kp, $\bar{K}^0n$, $\Sigma^+\pi^-$, and $\Sigma^-\pi^+$ channels in the vicinity of the resonance and found the A_4 coefficients shown in Table XI with their uncertainties. Also listed is the computed A_4 fit over the same momentum intervals from the computer analysis. The calculated value of A_4 is positive, since it comes mainly from the resonant term, the nonresonant D_3 amplitudes being small. Most experimental points are negative but with large uncertainty. The probability of there being this much or more $\cos^4\theta$ in the data is 10%. It is also clear that a relaxation of the constant-scattering-length assumption would not significantly improve the agreement of the $D_{5/2}$ possibility, since if this led to an enlarged $\bar{K}^0n$ bump, it would necessarily result in larger predicted values of A_4 in all channels, further conflicting with experiment. We conclude that the over-all probability that the resonance spin is $\frac{5}{2}$ is less than 1%.

E. Parameter Uncertainties

The uncertainty associated with each parameter may be obtained by inverting the second-derivative matrix of the χ^2 function. Let G be the complete error matrix. At the minimum, we have

$$\chi^2=\chi_{\min}{}^2+\tfrac{1}{2}\sum_{i,j}\left(\frac{\partial^2\chi^2}{\partial a_i\partial a_i}\right)_{\min}\delta a_i\delta a_j$$

$$+\text{higher derivative terms.}$$

Then with $M_{ij}=(1/2)(\partial^2\chi^2/\partial a_i\partial a_j)$ we have $G_{ij}=(M^{-1})_{ij}$. If the χ^2 space is strictly quadratic, this pro-

TABLE XI. Experimental and computed A_4 coefficients.

Reaction	Momentum interval (MeV/c)	A_4 (Experimental)	A_4 (Solution IX)
K^-p	380 to 420	-0.169 ± 0.219	$+0.070$
$\bar{K}^0n$	370 to 410	$+0.172\pm0.136$	$+0.050$
$\Sigma^+\pi^-$	380 to 410	-0.117 ± 0.117	$+0.115$
$\Sigma^-\pi^-$	380 to 410	-0.026 ± 0.106	$+0.115$

cedure for determining the error matrix can be shown to be equivalent to displacing one parameter by an amount which increases χ^2 by one after readjusting all other parameters. The displacement is then equal to the diagonal element of the error matrix, while the change in all other parameters yields the off-diagonal elements. Since our χ^2 space is far from quadratic in all directions over a region sufficiently large for χ^2 to change by one, these two methods are not equivalent. The first procedure of inverting the second-derivative matrix is clearly easier, but for several parameters yielded unreasonably small diagonal elements. For these, we employed the second procedure to obtain more meaningful errors. Our estimates for the diagonal errors of solution II are listed in the last column of Table IX. It is to be understood that because correlations are large and the χ^2 space deviates considerably from a quadratic in the region of the minimum, these diagonal errors are to be regarded with caution and should be used only as rough guides. The differences between solutions I to IV which involve different assumptions in the parametrization also give an indication as to the parameter uncertainties. Furthermore, as stated previously, ambiguities exist among the smaller amplitudes which yield χ^2 values higher than those reported but yet not so high as to be unacceptable. More precise experiments in this region may well show a preference for another of these solutions.

Lastly, there are uncertainties not contained in the computer analysis arising from the momentum resolution of the experiment. Since only the resonance parameters are rapidly varying, only they should be affected significantly. Different channels have different resolution widths, so that the over-all resolution is difficult to determine quantitatively. Furthermore, much of the information concerning the resonance comes from interference terms involving resonant and nonresonant amplitudes. These effects extend over a broader momentum range than the cross-section enhancements which come from the squared resonance amplitude. There is also an arbitrariness of 5 MeV/c in the choice of momentum intervals and an uncertainty of less than that in the incoming central momentum. Over all, we estimate the uncertainty due to experimental resolution to be less than 2 MeV, both for the resonant energy and for the width.

IX. DISCUSSION AND CONCLUSION

In this section we discuss the assumptions that enter into the analysis, and the degree to which our conclusion of negative $KN\Sigma$ parity is dependent upon these assumptions.

In parametrizing the computer analysis, we have assumed strict validity of charge independence. This has been found to agree with $K^- - D$ experiments to a precision of about 5%.[29,13] Furthermore, no inconsistencies with charge independence have occurred in the considerable body of experimental data on strange particles. The agreement of this experiment with charge independence further strengthens the assumption.[30] On the other hand, mass differences among the various charge multiplets are quite large and comparable to the half-width of the resonance. Deviations from charge independence sufficiently large as to be evident may, therefore, be expected due to these mass differences. A naive but perhaps not completely meaningless calculation of mass-difference effects might proceed as follows. Assume that all three $\Sigma\pi$ states are equally coupled to the resonance. The only difference in the decay rate of the resonance into each $\Sigma\pi$ channel would be due to the centrifugal barrier and phase-space factor for a D-wave resonance by Eq. (21). At resonance we have $P_\Sigma = 265$ MeV/c, so that $KR \lesssim 1$ for a reasonable radius of interaction, $R \lesssim \lambda_\pi/2$. The momentum dependence of Γ is then closely approximated by $\Gamma \propto K^5$ (which also agrees best with the computer fit). The momentum differences between the various $\Sigma\pi$ states then lead to a branching ratio $\Sigma^+:\Sigma^0:\Sigma^- = 1.12:1.12:1$. This is in the right direction to account for the experimental resonance branching ratio, although the observed differences are somewhat larger. (Of course, different Σ ratios can also be obtained by introduction of a nonresonant D_3 amplitude in $I=1$.) One may further remark that the momentum difference between $\Sigma\pi$ and $\bar{K}N$ channels would lead to a branching ratio $\Sigma\pi/\bar{K}n = 1.66$ if they had equal coupling. Experimentally, we find 1.86 ± 0.2. It would, thus, appear that all two-body channels are equally coupled to the resonance.

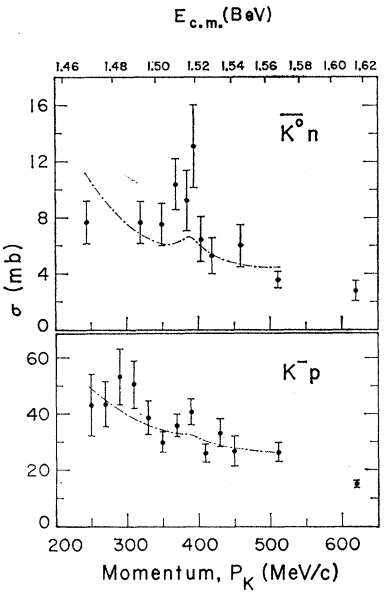

FIG. 41. The $\bar{K}^0 n$ and $K^- p$ cross sections as a function of momentum. The curves are computed under the assumption that Y_0^* (1520) is a $J=\frac{5}{2}$ resonance. The only data used by the computer which is not well fit by this assumption is the $\bar{K}^0 n$ cross section.

[29] L. W. Alvarez, see Ref. 2.

[30] Because of the experimental difficulties associated with the $\Sigma^0\pi^0$ channel, we do not regard the rather poor fit to the P–E ratio for $\Sigma^0\pi^0$ to indicate a violation of charge independence.

TABLE XII. Comparison of the S-wave parameters for our solution I with the Humphrey-Ross solutions 1 and 2.

Humphrey-Ross solutions		400 MeV/c region values	
Solution 1	Solution 2	Symbols	Solution I
-0.22 ± 1.07	-0.59 ± 0.46	a_0	-0.08 ± 0.5
2.74 ± 0.31	0.96 ± 0.17	b_0	3.13 ± 0.8
0.02 ± 0.33	1.20 ± 0.06	a_1	0.02 ± 0.08
0.38 ± 0.08	0.56 ± 0.15	b_1	0.46 ± 0.04
0.40 ± 0.03	0.39 ± 0.02	$r_{S1}{}^{\Lambda\pi}$	0.29 ± 0.03
$\approx 90^{a}$	$\approx -90^{a}$	ϕ_{S0-S1} (deg)	-104 ± 7

[a] This angle was not actually used as the sixth parameter by Humphrey and Ross. The values shown are rough predicted extrapolations for this phase based on their solutions.

A second assumption concerns the number of partial waves that contribute significantly in the region of the resonance. Note that at resonance the K^-p c.m. momentum is 245 MeV/c. Even for a radius of interaction as large as $\lambda\!\!\!^{-}_{\pi}$ this gives $KR=1.7$ at resonance. Thus, it is highly unlikely that amplitudes beyond D waves contribute appreciably. The data reflect this in that satisfactory fits are obtainable with nonresonant S and P waves only. In this connection it is instructive to consider the other known boson-nucleon interactions. The first $\pi-N$ resonance, $N^*(1238)$, occurs at a c.m. momentum of 233 MeV/c, 5% lower than $Y_0^*(1520)$. Careful investigation of this interaction in the resonance region leads to a satisfactory description in terms of S and P amplitudes only. Similarly, the K^+-p interaction appears to be purely S wave below 600 MeV/c, while the available K^+-n data is in satisfactory agreement with S and P waves. Furthermore, the nonresonant amplitudes at these momenta can be reasonably well described by constant scattering lengths. It is, thus, plausible to generalize that boson-nucleon interactions are not pathological.

We have found that the various interference effects associated with the resonant amplitude are well described by a Breit-Wigner form with a momentum dependence of the partial widths by $\Gamma\propto K^5$. Since the resonance is narrow, the precise momentum dependence of Γ is not crucial. A more elaborate analysis involving the introduction of different momentum dependences of the partial widths in each channel could perhaps improve the positive $KN\Sigma$ parity fit somewhat. However, the parity conclusion is based on a very gross measurement of the sign of an interference between two large amplitudes which dominate the reaction; it is in no way a subtle effect. Hence, such embellishments of the channel widths cannot weaken the conclusion significantly.

Let us consider now the parametrization of the nonresonant amplitudes in terms of constant scattering lengths. This is assumed primarily in order to provide a momentum continuity for the amplitudes. The precision of the experiment is not such as to warrant introduction of effective-range parameters, as is apparent from the fact that constant scattering lengths fit quite well over the momentum region investigated. This is not to be construed as meaning that effective-range effects are absent. Table XII compares our S-wave parameters to those obtained by Humphrey and Ross at lower energy.[1] Our phase angle ϕ_{S0-S1} agrees with their solution 2, while the scattering lengths in general are in closer agreement with solution 1. Akiba and Capps[23] have shown that this situation could arise from the presence of reasonable effective-range terms. When both experiments are done with greater precision and the properties of $Y_0^*(1405)$ are better established, perhaps meaningful effective-range parameters can be extracted from a comparison of the two experiments.

The general method we use is similar to that originally discussed[10] and later improved[17] by Capps. We have, however, formulated the problem in such a way as to permit an analysis of the over-all K^-p interaction utilizing all measurable data. Treating this broader problem has necessitated the introduction of dynamical assumptions. On the other hand, the parity arguments are to a large extent independent of these assumptions. This has been emphasized by Capps.[17] To demonstrate this we have minimized χ^2, using only the $\Sigma^+\pi^-$ data and only over a momentum interval ±60 MeV/c surrounding the resonance. This removes the assumption of charge independence and considerably relaxes those of constant scattering lengths and energy dependence of partial widths. Again the data strongly favor a D-wave $\Sigma\pi$ resonant state, the χ^2 being 44.9 and 72.3 for negative and positive $KN\Sigma$, respectively, when $\chi^2=42$ is expected. The probability of positive $KN\Sigma$ parity satisfying even this limited data is 0.25%. The purpose of the computer analysis, however, has been not only to establish the Σ parity, but also to correlate with a minimum number of parameters a large body of data undergoing rapid and spectacular momentum variations. That the analysis can survive these many experimental hurdles gives us much more confidence in the parity conclusion than one might have by only fitting one channel.

The D-wave assignment for the incoming K^-p resonant state is very strongly favored by the computer fit. Here the assumption of constant scattering lengths enters into the analysis considerably more forcefully than in the $\Sigma\pi$ orbital-state identification. Relaxing this assumption would significantly lower χ^2 for solution VIII for the P_3 resonance possibility. However, it is clear from previous arguments that the data cannot be fitted with a P_3 resonance unless some very unlikely behavior is assumed for the nonresonant S and P_1 amplitudes.

A much more likely possibility is that $Y_0^*(1520)$ may be a $J=\frac{5}{2}$ resonance. Computer fits indicate that this has a probability of somewhat less than 1% of fitting the data, the only serious disagreements are (a) the inability of an incident D_5 resonance to reproduce the various angular distributions and simultaneously yield the resonant enhancement in the $\bar{K}^0n$ cross section and (b) the absence of $\cos^4\theta$ in the angular distributions. A

$J=\frac{5}{2}$ resonance would lead most naturally to the opposite conclusion concerning the Σ parity.

We should note that this experiment contains two nearly independent measurements, both clearly indicating negative $KN\Sigma$ parity. The stronger of the two involves $S-D_3$ interference and correlates $\cos^2\theta$ in the angular distribution with the $\sin\theta\cos\theta$ polarization term. The other involves P_3-D_3 interference correlating $\cos^3\theta$ terms in the angular distribution with the $\sin\theta$ and $\sin\theta\cos^2\theta$ polarization terms. Both of these experiments necessitate a knowledge of the helicity in Σ_0^+ decay previously measured.[8] A reversal of this sign would reverse the parity conclusion, apart from a very weak indication from Σ^0 polarization that would still favor negative $KN\Sigma$ parity.

Finally, the $KN\Lambda$ parity has been rather convincingly shown to be negative through experiments involving K^- capture in helium.[31,19] The relative $\Sigma-\Lambda$ parity is thus found to be even. Theoretical schemes for strange particles have generally been based on the assumption of even $\Sigma-\Lambda$ parity.

[31] M. Block, F. Anderson, H. Pevsner, E. Harth, J. Leitner, and H. Cohn, Phys. Rev. Letters **3**, 291 (1959); R. Dalitz and L. Liu, Phys. Rev. **116**, 1312 (1959). For the most recent summary of the experimental situation concerning the $KN\Lambda$ parity, see the reports of M. M. Block and of R. H. Dalitz in *Proceedings of the 1962 International Conference on High-Energy Physics at CERN* (CERN, Geneva, 1962).

ACKNOWLEDGMENTS

Many persons have contributed greatly to the experiment. We are indebted in particular to Professor L. W. Alvarez for his support and Dr. J. J. Murray for his design and execution of the K^- beam. Others who have contributed to the general K^- investigation are Professor D. H. Miller, Professor A. H. Rosenfeld, Dr. O. I. Dahl, and P. L. Bastien, J. P. Berge, and J. Kirz. Theoretical discussions and correspondence with Professor R. H. Capps, Professor R. H. Dalitz, Professor M. Gell-Mann, and Dr. H. P. Stapp have been very valuable in formulating the K^-p phenomenology. Dr. W. E. Humphrey and Dr. R. R. Ross gave frequent advice on the computer analysis. The help from our scanners, D. J. Church, C. Dudley, M. R. Kelly, C. Owens, and R. Tye in finding and analyzing the events is gratefully acknowledged.